The Astrophysical Journal, 882:30 (17pp), 2019 September 1 https://doi.org/10.3847/1538-4357/ab2b49
© 2019. The American Astronomical Society. All rights reserved.

Observations of Type Ia Supernova 2014J for Nearly 900 Days and Constraints on Its Progenitor System

Wenxiong Li[1], Xiaofeng Wang[1], Maokai Hu[2], Yi Yang[3], Jujia Zhang[4,5], Jun Mo[1], Zhihao Chen[1], Tianmeng Zhang[6], Stefano Benetti[7], Enrico Cappellaro[7], Nancy Elias-Rosa[8,9], Jordi Isern[8,9], Antonia Morales-Garoffolo[10], Fang Huang[5,11], Paolo Ochner[12], Andrea Pastorello[7], Andrea Reguitti[13], Leonardo Tartaglia[14], Giacomo Terreran[15], Lina Tomasella[7], and Lifan Wang[2,16]

[1] Physics Department and Tsinghua Center for Astrophysics (THCA), Tsinghua University, Beijing, 100084, People's Republic of China
wang_xf@mail.tsinghua.edu.cn
[2] Purple Mountain Observatory, Chinese Academy of Sciences, Nanjing 210034, People's Republic of China
[3] Department of Particle Physics and Astrophysics, Weizmann Institute of Science, Rehovot 76100, Israel
[4] Yunnan Astronomical Observatory of China, Chinese Academy of Sciences, Kunming, 650011, People's Republic of China
[5] Key Laboratory for the Structure and Evolution of Celestial Objects, Chinese Academy of Sciences, Kunming 650011, People's Republic of China
[6] National Astronomical Observatory of China, Chinese Academy of Sciences, Beijing, 100012, People's Republic of China
[7] INAF—Osservatorio Astronomico di Padova, Vicolo dell'Osservatorio 5, I-35122 Padova, Italy
[8] Institute of Space Sciences (ICE, CSIC), Campus UAB, Carrer de Can Magrans s/n, E-08193 Barcelona, Spain
[9] Institut d'Estudis Espacials de Catalunya (IEEC), c/Gran Capitá 2-4, Edif. Nexus 201, E-08034 Barcelona, Spain
[10] Department of Applied Physics, University of Cádiz, Campus of Puerto Real, E-11510, Cádiz, Spain
[11] Department of Astronomy, School of Physics and Astronomy, Shanghai Jiao Tong University, Shanghai 200240, People's Republic of China
[12] Dipartimento di Fisica e Astronomia G. Galilei, Universita' di Padova, Vicolo dell'Osservaotio 3, I-35122, Padova, Italy
[13] Departamento de Ciencias Fisicas, Universidad Andrés Bello, Fernandez Concha, 700, Santiago, Chile
[14] Department of Astronomy, Stockholm University, SE-10691 Stockholm, Sweden
[15] Center for Interdisciplinary Exploration and Research in Astrophysics (CIERA) and Department of Physics and Astronomy, Northwestern University, Evanston, IL 60208, USA
[16] George P. and Cynthia Woods Mitchell Institute for Fundamental Physics & Astronomy, Texas A. & M. University, Department of Physics and Astronomy, 4242 TAMU, College Station, TX 77843, USA
Received 2019 April 28; revised 2019 June 13; accepted 2019 June 15; published 2019 August 28

Abstract

We present extensive ground-based and *Hubble Space Telescope* (*HST*) photometry of the highly reddened, very nearby SN Ia 2014J in M82, covering the phases from 9 days before to about 900 days after the *B*-band maximum. SN 2014J is similar to other normal SNe Ia near the maximum light, but it shows flux excess in the *B* band in the early nebular phase. This excess flux emission can be due to light scattering by some structures of circumstellar materials located at a few 10^{17} cm, consistent with a single-degenerate progenitor system or a double-degenerate progenitor system with mass outflows in the final evolution or magnetically driven winds around the binary system. At $t \sim +300$ to $\sim+500$ days past the *B*-band maximum, the light curve of SN 2014J shows a faster decline relative to the ^{56}Ni decay. That feature can be attributed to the significant weakening of the emission features around [Fe III] λ4700 and [Fe II] λ5200 rather than the positron escape, as previously suggested. Analysis of the *HST* images taken at $t > 600$ days confirms that the luminosity of SN 2014J maintains a flat evolution at the very late phase. Fitting the late-time pseudobolometric light curve with radioactive decay of ^{56}Ni, ^{57}Ni, and ^{55}Fe isotopes, we obtain the mass ratio ^{57}Ni/^{56}Ni as 0.035 ± 0.011, which is consistent with the corresponding value predicted from the 2D and 3D delayed-detonation models. Combined with early-time analysis, we propose that delayed-detonation through the single-degenerate scenario is most likely favored for SN 2014J.

Key words: supernovae: general – supernovae: individual (SN 2014J)

Supporting material: machine-readable table

1. Introduction

SNe Ia are important tools to measure cosmological expansion (Riess et al. 1998). The progenitors of SNe Ia are believed to arise from a white dwarf (WD) inhabiting a binary system, with a mass close to the Chandrasekhar limit (Hoyle & Fowler 1960). However, the explosion mechanisms and binary evolution scenarios for SNe Ia are not well understood (Howell 2011; Maoz et al. 2014). The two common scenarios include (i) double-degenerate (DD) with one white dwarf tidally disrupting the WD companion and accreting its material (Iben & Tutukov 1984; Webbink 1984), and (ii) single-degenerate (SD) where the WD accretes matter from a main-sequence star (van den Heuvel et al. 1992), a subgiant (Han & Podsiadlowski 2004), a helium star (Wang et al. 2009; Geier et al. 2013) or a red giant companion (Whelan & Iben 1973; Nomoto 1982; Patat et al. 2011). One prediction of the SD scenario is that a considerable amount of circumstellar material (CSM) should be accumulated around the progenitor system via stellar wind of a companion star or successive nova eruptions, although the DD and core-degenerate models are also argued to be able to form nearby CSM (Levanon et al. 2015; Soker 2015).

The CSM formed by outflowing materials would result in blueshifted and evolving narrow interstellar absorption features such as the Na I doublet. Variable Na I D absorption was initially reported by Patat et al. (2007) in the spectra of SN 2006X. After that, several SNe Ia also showed variations in the Na I D absorption, including SN 2007le (Simon et al. 2009) and PTF 11kx (Dilday et al. 2012). There are also some statistical studies showing blueshifted narrow absorption features of Na I

D in the high-resolution spectra of some SNe Ia (Sternberg et al. 2011; Maguire et al. 2013; Sternberg et al. 2014), which are associated with the subclass characterized by higher photospheric velocities (Wang et al. 2009a, 2013). Both results indicate that some SNe Ia are surrounded by CSM, favoring their SD progenitor system origin (Foley et al. 2012; Hachinger et al. 2017).

Another effect due to the presence of surrounding CSM is the extinction along the line of sight and the scattering of the SN light. The CSM can scatter photons back to the line of sight and hence reduce the total extinction and R_V (Wang 2005; Goobar 2008). Based on analysis of a large sample of Na I doublet absorption features in SN Ia spectra and light-curve evolution in the early nebular phase, Wang et al. (2018) provided evidence that SNe Ia with higher photospheric velocity (HV) likely have CS dust at a distance of about 2×10^{17} cm, implying that this subclass may have a single-degenerate origin.

Very early observations of SNe Ia are promising ways to constrain their progenitor systems. Different scenarios explain the diversity of the early evolutions of SNe Ia (Kasen 2010; Maeda et al. 2014; Piro & Morozova 2016; Jiang et al. 2017). A growing number of SNe Ia with early-phase observations have been studied (Zheng et al. 2013; Cao et al. 2015; Marion et al. 2016; Hosseinzadeh et al. 2017; Miller et al. 2018). SN 2018oh is the only spectroscopically confirmed normal SN Ia with *Kepler Space Telescope* high-cadence photometry since explosion (Li et al. 2019). Detailed studies reveal there is a bump in the early light curve of SN 2018oh that may stem from non-degenerate companion interaction (Dimitriadis et al. 2019) or ^{56}Ni radiation from the outer part of the ejecta (Shappee et al. 2019).

The other way to distinguish the SD and DD scenario is to observe late-time evolution of SN Ia. The early-time light curve of SN Ia is powered by the radioactive decay chain $^{56}\mathrm{Ni} \rightarrow {}^{56}\mathrm{Co} \rightarrow {}^{56}\mathrm{Fe}$ with half-lives $t_{1/2} \sim 6$ and 77 days, respectively. With the expansion of the ejecta, the column density decreases as t^{-2}. Therefore, after $t \sim 200$ days, the ejecta are almost transparent to γ-rays, and positron emission begins to dominate the heating process (Arnett 1979; Milne et al. 1999). Assuming complete positron trapping, the light curve at this stage should follow the decay rate of ^{56}Co, i.e., 0.98 mag per 100 days.

At the very late phase, the light curves of some SNe Ia are found to flatten compared to the ^{56}Co decay, including SN 1992A (Cappellaro et al. 1997), SN 2003hv (Leloudas et al. 2009), SN 2011fe (Kerzendorf et al. 2014; Shappee et al. 2017), SN 2012cg (Graur et al. 2016), ASASSN-14lp (Graur et al. 2018a), and SN 2015F (Graur et al. 2018b). Seitenzahl et al. (2009) suggested that the additional energy should come from the long-lived decay chains $^{57}\mathrm{Co} \rightarrow {}^{57}\mathrm{Fe}$ ($t_{1/2} \sim 272$ days) or $^{55}\mathrm{Fe} \rightarrow {}^{55}\mathrm{Mn}$ ($t_{1/2} \sim 1000$ days). The ratio of these isotopes relative to ^{56}Ni depends on the density of the progenitor, which is different in SD and DD models (Röpke et al. 2012). Higher $^{57}\mathrm{Ni}/{}^{56}\mathrm{Ni}$ mass ratios are predicted by WD models of higher central density. This is because ^{57}Ni is a neutron-rich isotope that has a higher abundance in neutron-rich environments such as near-Chandrasekhar-mass, delayed-detonation explosion models (Khokhlov 1989; Seitenzahl et al. 2013), as expected for the single-degenerate channel. Therefore, these ratios can provide clues to the progenitor models.

There are also other explanations for the flattening of the light curves. For example, an unresolved light echo, due to scattering of the SN light by nearby CSM or interstellar dust, can naturally increase the luminosity. Fransson & Kozma (1993) suggested that the recombination and cooling timescale is longer than radioactive decay as a result of decreasing density of the ejecta, the so-called "freeze-out" effect, which can make the light curves flat at late time. Combining this "freeze-out" effect with the ^{56}Co decay, Fransson & Jerkstrand (2015) and Kerzendorf et al. (2017) provided reasonable explanations for the very-late-time spectrum and light curve of SN 2011fe.

SN 2014J is a very nearby SN Ia, the distance being ~3.53 Mpc (Dalcanton et al. 2009). This provides an excellent opportunity to study its progenitor through the detection of dusty environment and the analysis of late-time light-curve evolution. This bright SN has been followed up by many instruments, covering γ-rays by *INTEGRAL* (Churazov et al. 2014, 2015; Diehl et al. 2014, 2015; Isern et al. 2016) and *Suzaku* (Terada et al. 2016), X-rays (Margutti et al. 2014), UV (Foley et al. 2014; Brown et al. 2015), optical (Goobar et al. 2015; Siverd et al. 2015; Bonanos & Boumis 2016), near-infrared (Marion et al. 2015; Vacca et al. 2015; Sand et al. 2016), mid-infrared (MIR) (Telesco et al. 2015; Johansson et al. 2017), and radio bands (Pérez-Torres et al. 2014); polarimetric observations have also been presented (Kawabata et al. 2014; Patat et al. 2015; Porter et al. 2016; Yang et al. 2018b).

The heavy reddening toward SN 2014J has inspired plentiful studies focusing on its dusty environment. With the UV and optical light curves and spectra obtained with *Swift*, Brown et al. (2015) concluded that the large reddening mainly originates from the absorption features of the interstellar medium (ISM), which is also confirmed by the light echo emerging after ~200 days (Crotts 2015; Yang et al. 2017). By measuring the continuum polarization of SN 2014J, Patat et al. (2015) came to a similar conclusion. Amanullah et al. (2014) found that the unusual reddening behavior seen in SN 2014J can be explained by non-standard ISM dust with $R_V = 1.4 \pm 0.1$ or by power-law extinction of CSM (Wang 2005). Foley et al. (2014) used a hybrid model including both ISM and CSM to explain the extinction curve. Graham et al. (2015b) identified time-varying potassium lines and attributed them to the CSM origin. Based on the *Spitzer* MIR data, Johansson et al. (2017) placed an upper limit on the pre-existing circumstellar dust, with $M_{\mathrm{CSM}} \leqslant 10^{-5}\ M_{\odot}$ and a distance of $r \sim 10^{17}$ cm from the SN. By studying the late-time polarimetry of SN 2014J with the *Hubble Space Telescope* (*HST*) ACS/WFC observations, Yang et al. (2018b) concluded that at least $\sim 10^{-6}\ M_{\odot}$ of circumstellar dust is located at a distance of 5×10^{17} cm from SN 2014J.

Yang et al. (2018a) also analyzed the late-time *HST* photometry and found that both the F665W-band and the bolometric light curve of SN 2014J exhibited flattening behavior. Recently, Graur (2019) confirms the late-time flattening in F555W and F438W bands of *HST* Wide Field Camera 3 UVIS channel (WFC3/UVIS).

In this paper, we present extensive photometry of SN 2014J from ground-based telescopes and *HST*, and analyze the light-curve evolution by comparison with other well-observed SNe Ia. Photometric observations are addressed in Section 2. In Section 3, we examine the light curves near the maximum light and in the early nebular phase. In Section 4, we examine the

Table 1
Photometric Standards in the SN 2014J Field

Num.	α(J2000)	δ(J2000)	*U* (mag)	*B* (mag)	*V* (mag)	*R* (mag)	*I* (mag)
1	148.8956	69.6487	10.785(0.003)	10.640(0.002)	10.077(0.001)	9.742(0.002)	9.447(0.001)
2	149.1370	69.6547	12.808(0.005)	12.849(0.004)	12.303(0.002)	11.953(0.004)	11.621(0.003)
3	148.7262	69.6155	13.676(0.009)	13.783(0.006)	13.306(0.003)	12.994(0.006)	12.693(0.005)
4	148.8436	69.6332	14.231(0.014)	14.326(0.009)	13.816(0.004)	13.468(0.007)	13.122(0.006)
5	148.7226	69.6583	15.204(0.024)	14.930(0.012)	14.213(0.006)	13.795(0.010)	13.412(0.008)
6	148.9691	69.7350	15.717(0.038)	15.536(0.018)	14.850(0.008)	14.421(0.014)	14.005(0.012)
7	148.9235	69.6663	16.066(0.063)	15.977(0.036)	15.232(0.017)	14.745(0.032)	14.326(0.027)
8	148.8290	69.7257	17.625(0.186)	17.262(0.072)	16.499(0.030)	15.986(0.052)	15.603(0.044)
9	148.8551	69.6893	17.800(0.207)	17.374(0.078)	16.506(0.030)	15.989(0.052)	15.524(0.044)
10	148.8188	69.6409	16.174(0.069)	16.367(0.042)	16.141(0.021)	16.037(0.043)	15.876(0.035)

Note. Uncertainties, in units of 0.001 mag, are 1σ.

very-late-time evolution and explore its possible origins. We discuss and conclude in Section 5.

2. Observations

2.1. Ground-based Photometry

Our ground-based optical photometry of SN 2014J was obtained with the following telescopes: (1) the 0.8 m THCA-NAOC Telescope (TNT; Huang et al. 2012) at Beijing Xinglong Observatory (BAO) in China; (2) the 2.4 m Lijiang Telescope (LJT) of Yunnan Astronomical Observatory (YNAO); (3) the 2.56 m Nordic Optical Telescope (NOT) of Roque de los Muchachos Observatory in the Canary Islands; (4) the 0.8 m Telescopi Joan Oró (TJO) located at the Montsec Astronomical Observatory; (5) the Asiago Copernico 1.82 m telescope (COP) with AFOSC; (6) the Asiago Schmidt 67/92 (SCH) with SBIG and (7) the 3.58 m Telescopio Nazionale Galileo (TNG) with LRS. All CCD images were corrected for bias and flat field. Template subtraction has been applied to improve photometry to all images. The latest ground-based image with signals was taken with the Asiago Copernico 1.82 m telescope (COP) at 434 days relative to the *B*-band maximum light. And the template image used for galaxy subtraction was obtained on 2017 June 19th, corresponding to about 1234.0 days after the maximum light. This late-time COP *V*-band image with galaxy subtraction is shown in Figure 6(b), together with the F555 *HST* images. The SN was imaged in the *UBVRI* bands with TNT, LJT, TJO, TNG, and COP, and *BVRI* bands with NOT and SCH.

The photometry data were analyzed with the open-source online photometry and astrometry codes SWARP (Bertin et al. 2002), SCAMP (Bertin 2006), and SExtractor (Bertin & Arnouts 1996). We performed aperture photometry on the template-subtracted SN images with SExtractor. The SN instrumental magnitudes were calibrated using Landolt standards stars, and the final flux-calibrated magnitudes are listed in Table 1. The photometric uncertainties include the Poisson noise of the signal and the photon noise of the local background. The field of SN 2014J taken with LJT is displayed in Figure 1, the latest template-subtracted image taken by COP on +434 days in the *V* band is displayed in Figure 6(b), and the final flux-calibrated magnitudes are listed in Table 2.

2.2. HST Photometry

Very-late-time photometry of SN 2014J can be extracted from the archival images obtained through the *HST* WFC3/UVIS programs (Proposal 13626, PI: Lawrence, 14146, PI: Lawrence and 14700, PI: Sugerman). The wavelength coverage of F438W and F555W filters is similar to that of the *B* and *V* bands, respectively. The information on *HST* observations is given in Table 3.

When multiple exposures were available at similar phases in the same filter, we combined them (using SCAMP and SWARP). As for the ground-telescope images, we performed aperture photometry with SExtractor. For each image, we chose a 6 pixel aperture for the photometry, which does not include the flux from the light echo. However, for the last-epoch image obtained in the *HST* F438W filter at +881 days from the maximum light (when the SN had faded enough), we adjusted the aperture size to 4 pixels to avoid background contamination. We applied aperture corrections according to Deustua et al. (2017) to calculate the total flux of the SN. The photometric error added in quadrature includes uncertainties in Poisson noise, background noise, and aperture correction. The resulting photometric analysis is presented in Table 4.

3. Evolution During the First 5 Months

3.1. Light/Color Curves

Figure 2 shows our *UBVRI* light curves of SN 2014J obtained during the first 5 months of evolution. From a low-order polynomial fit to the near-maximum light curve, we derive $B_{\max} = 11.92 \pm 0.03$ mag, $t_{B\max} = \mathrm{JD}\ 2456690.1 \pm 0.1$ day, and $\Delta m_{15}(B)_{\rm obs} = 0.98 \pm 0.01$ mag. Our measurement is consistent with the result reported in Foley et al. (2014) and Srivastav et al. (2016). However, SN 2014J suffers from large reddening, which shifts the effective wavelength redward. The intrinsic decline rate parameter derived by Phillips et al. (1999) is

$$\Delta m_{15}(B)_{\rm true} \simeq \Delta m_{15}(B)_{\rm obs} + 0.1 \times E(B-V)_{\rm obs}.$$

According to Schlafly & Finkbeiner (2011), the Galactic reddening toward M82 is $E(B-V)_{\rm MW} = 0.138$ mag. However, as pointed by Dalcanton et al. (2009), this estimate may be strongly contaminated by point-source emission from M82 itself. They suggested a lower value of $E(B-V)_{\rm MW} = 0.059$ mag on the Schlegel et al. (1998) scale, which is close to the value used by Amanullah et al. (2015). Converting to the Schlafly & Finkbeiner (2011) scale with a factor of 0.86, the final Galactic reddening adopted in our analysis is $E(B-V)_{\rm MW} = 0.052$ mag, with the classic reddening law of $R_V = 3.1$ (Cardelli et al. 1989), consistent with that used by Foley et al. (2014).

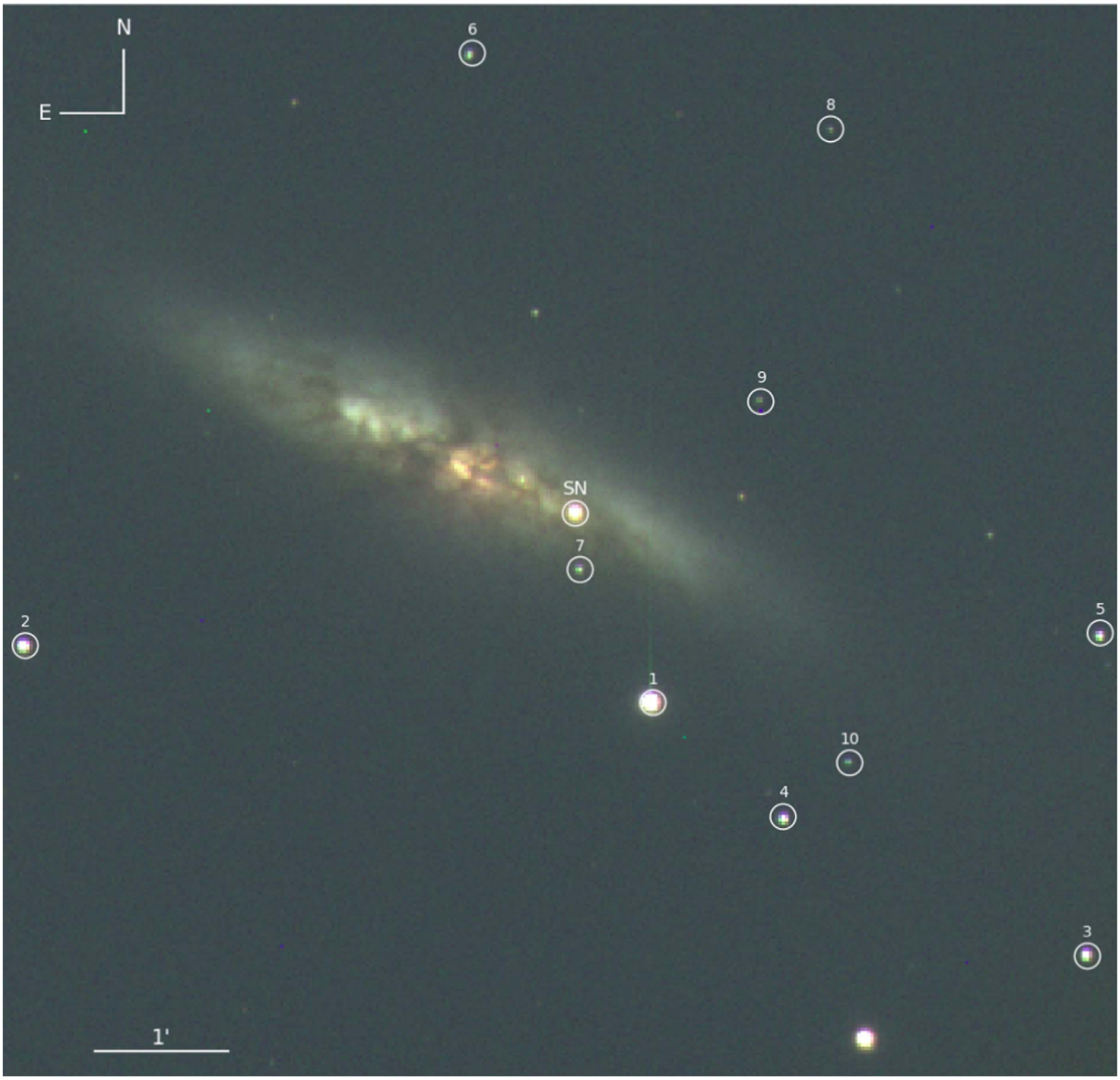


Figure 1. SN 2014J in M82. The composite image was produced by combining *B*(blue)-, *V* (green)-, and *R* (red)-band images obtained with LJT on 2014 January 22.8 UT. The reference stars listed in Table 1 are numbered. North is up and east is to the left.

Several studies discussed the total reddening toward SN 2014J but did not come to a consistent conclusion (see below). In our study, we adopt a model-independent reddening $E(B-V)_{\rm obs} = 1.19 \pm 0.14$ mag with a reddening law of $R_V = 1.64 \pm 0.16$, as in Foley et al. (2014). Therefore, the reddening-corrected $\Delta m_{15}(B)_{\rm true}$ is $\simeq$1.10 $\pm$ 0.02 mag for SN 2014J, similar to those of SN 2003du (1.04 ± 0.02 mag, Anupama et al. 2005; 1.02 ± 0.05 mag, Stanishev et al. 2007), SN 2005cf (1.07 ± 0.03 mag, Wang et al. 2009b), and SN 2011fe (1.18 ± 0.03 mag, Zhang et al. 2016).

Figure 3 shows the comparison of the *B*- and *V*-band light curves of SN 2014J with those of SN 2003du, SN 2005cf, and SN 2011fe. We note that the *B*-band light curve of SN 2014J becomes somewhat flattened at $t \sim +40$ days, and shows emission excess relative to the compared SNe Ia with similar $\Delta m_{15}(B)$. The deviation in the *B* band is evident, while this trend is less prominent in the *V* band. The decline rates measured during the period $t \sim$ 50–110 days are tabulated in Table 5. Previous works suggest that SN 2014J is a normal SN Ia, except for the higher velocity of the ejecta (Zhang et al. 2018); this flattening effect may be related to CS dust scattering of the SN light that is commonly seen in the high-velocity subclass, as suggested by Wang et al. (2018).

In the following analysis, we attempt to model the *B*-band emission excess with additional SN photons scattered back by a dusty medium, i.e., a light echo. In this scenario, we adopt a single scattering approximation following the procedure described in Patat (2005). If d is the distance between SN 2014J and the observer, we can assume that $c\Delta t \ll d$, where c is the speed of light and Δt is the duration of the SN radiation. As d is much larger than other geometrical quantities considered here, at any moment, the distribution of the scattered photons along the line of sight can be approximated as a paraboloid with the SN locating at its focus. $L_\lambda(t)$ is the luminosity of the SN at wavelength λ and $F_{{\rm SN},\lambda} = L_\lambda(t)/4\pi d^2$ is the corresponding flux. Thus, the flux of the scattered light at

Table 2
Ground-based Photometry of SN 2014J

UT Date	[a]Epoch	*U* (mag)	*B* (mag)	*V* (mag)	*R* (mag)	*I* (mag)	Telescope
2014 Jan 22.9	−9.7	13.31(04)	12.88(02)	11.63(03)	10.91(06)	10.49(05)	LJT
2014 Jan 23.9	−8.7	13.01(04)	12.62(02)	11.39(03)	10.62(06)	10.19(03)	LJT
2014 Jan 24.8	−7.8	12.79(04)	12.43(02)	11.21(02)	10.48(06)	10.08(03)	LJT
2014 Jan 25.1	−7.5	12.72(03)	...	11.13(03)	...	...	TJO
2014 Jan 25.9	−6.7	12.69(04)	12.29(02)	11.07(01)	10.40(06)	9.96(03)	LJT
2014 Jan 25.9	−6.7	12.70(02)	12.33(04)	11.11(01)	10.47(01)	10.04(03)	COP
2014 Jan 26.0	−6.6	12.72(04)	12.22(02)	11.12(01)	10.40(02)	9.95(02)	TNG
2014 Jan 26.9	−5.7	12.56(04)	12.16(02)	10.93(01)	10.30(05)	9.88(03)	LJT
2014 Jan 27.7	−4.9	...	12.14(02)	10.84(01)	10.23(04)	9.85(03)	TNT
2014 Jan 27.9	−4.7	12.53(05)	12.08(02)	10.86(01)	10.24(05)	9.80(03)	LJT
2014 Jan 28.6	−4.0	...	12.04(02)	10.75(01)	10.16(04)	9.81(02)	TNT
2014 Jan 28.9	−3.7	12.47(04)	12.02(02)	10.78(01)	10.19(05)	9.86(03)	LJT
2014 Jan 29.9	−2.7	12.41(04)	11.95(02)	10.71(01)	10.13(05)	9.77(03)	LJT
2014 Jan 30.9	−1.7	12.41(04)	11.92(02)	10.65(01)	10.12(05)	9.75(03)	LJT
2014 Jan 31.9	−0.7	12.39(04)	11.91(02)	10.62(02)	10.10(05)	9.79(03)	LJT
2014 Feb 01.9	+0.3	12.45(04)	11.89(02)	10.61(02)	10.07(05)	9.79(02)	LJT
2014 Feb 02.8	+1.2	12.48(04)	11.89(02)	10.58(01)	10.08(05)	9.80(02)	LJT
2014 Feb 04.9	+3.3	12.58(04)	11.99(02)	10.63(01)	10.11(05)	9.88(02)	LJT
2014 Feb 09.1	+7.5	12.87(07)	12.27(02)	10.75(03)	10.25(02)	10.14(02)	TJO
2014 Feb 09.7	+8.1	...	12.37(04)	10.72(03)	10.30(04)	10.17(03)	TNT
2014 Feb 11.2	+9.6	...	12.41(02)	10.80(03)	10.38(02)	10.23(02)	TJO
2014 Feb 12.1	+10.5	13.17(07)	12.48(03)	10.90(03)	10.46(03)	10.32(01)	TJO
2014 Feb 12.6	+11.0	13.24(07)	12.59(03)	10.92(02)	10.51(04)	10.29(02)	TNT
2014 Feb 14.7	+13.1	...	12.70(05)	10.97(04)	10.75(05)	10.35(03)	TNT
2014 Feb 15.5	+13.9	13.60(07)	12.84(04)	11.08(02)	10.73(04)	10.44(03)	TNT
2014 Feb 17.0	+15.4	13.63(05)	13.00(02)	11.09(02)	10.76(02)	10.43(01)	TJO
2014 Feb 20.0	+18.4	14.12(04)	13.29(02)	11.23(03)	10.80(02)	10.40(03)	TJO
2014 Feb 22.1	+20.5	14.33(07)	13.51(05)	11.32(03)	10.83(01)	10.33(03)	TJO
2014 Feb 23.1	+21.5	14.45(08)	13.60(04)	11.36(03)	10.85(01)	10.31(03)	TJO
2014 Feb 24.1	+22.5	14.54(05)	13.69(04)	11.38(02)	10.84(02)	10.31(01)	TJO
2014 Feb 27.9	+26.3	14.75(05)	14.04(03)	...	...	...	TJO
2014 Feb 28.6	+27.0	14.86(06)	14.02(03)	11.56(02)	10.83(04)	10.15(03)	TNT
2014 Mar 01.6	+28.0	15.06(05)	14.14(03)	11.63(02)	10.89(04)	10.19(03)	TNT
2014 Mar 02.5	+28.9	15.06(06)	14.22(03)	11.66(03)	10.90(05)	...	TNT
2014 Mar 04.8	+31.2	15.17(05)	14.34(03)	11.79(02)	11.02(05)	10.23(03)	TNT
2014 Mar 05.0	+32.4	...	14.47(03)	11.87(01)	11.13(03)	10.33(03)	TJO
2014 Mar 05.8	+32.2	...	14.46(03)	11.87(02)	11.09(05)	10.27(03)	TNT
2014 Mar 07.8	+34.2	15.23(03)	14.57(03)	11.99(03)	11.29(04)	10.46(04)	TJO
2014 Mar 09.8	+36.2	15.41(04)	14.65(03)	12.15(03)	11.41(02)	10.60(01)	TJO
2014 Mar 10.8	+37.2	15.40(04)	14.75(03)	12.18(02)	11.48(02)	10.66(01)	TJO
2014 Mar 11.1	+37.5	15.35(20)	14.71(03)	12.29(03)	11.46(04)	10.56(03)	COP
2014 Mar 12.0	+38.4	15.57(02)	14.77(02)	12.22(03)	11.54(02)	10.72(02)	TJO
2014 Mar 13.0	+39.4	15.56(05)	14.79(02)	12.26(02)	11.58(03)	10.82(01)	TJO
2014 Mar 13.6	+40.0	...	14.83(03)	12.28(03)	11.55(05)	10.81(03)	TNT
2014 Mar 13.8	+40.2	...	14.84(02)	12.31(03)	11.62(02)	10.87(02)	TJO
2014 Mar 14.6	+41.0	15.66(08)	14.84(03)	12.33(02)	11.62(05)	10.82(03)	TNT
2014 Mar 15.5	+41.9	15.76(09)	14.87(04)	12.38(02)	11.66(05)	10.86(03)	TNT
2014 Mar 19.5	+45.9	15.81(06)	14.90(03)	12.51(02)	11.82(05)	11.09(03)	TNT
2014 Mar 20.5	+46.9	15.86(06)	14.96(03)	12.52(02)	11.84(05)	11.13(03)	TNT
2014 Mar 22.5	+48.9	15.83(06)	14.95(03)	12.60(02)	11.92(05)	11.22(03)	TNT
2014 Mar 23.0	+49.4	15.84(04)	14.98(02)	12.59(03)	11.95(02)	11.30(01)	TJO
2014 Mar 25.5	+51.9	15.82(08)	14.96(03)	12.67(02)	12.02(05)	11.35(03)	TNT
2014 Mar 26.5	+52.9	15.85(11)	...	12.71(02)	12.06(05)	11.40(03)	TNT
2014 Mar 27.9	+54.3	15.90(04)	...	12.78(03)	12.12(02)	11.54(02)	TJO
2014 Mar 28.6	+55.0	15.91(19)	15.00(03)	12.77(02)	12.13(05)	11.49(03)	TNT
2014 Mar 29.5	+55.9	15.98(07)	15.06(03)	12.77(02)	12.14(05)	11.51(03)	TNT
2014 Mar 30.5	+56.9	16.08(07)	15.05(03)	12.83(02)	12.17(05)	11.58(03)	TNT
2014 Apr 01.0	+58.4	16.07(13)	15.04(12)	12.98(04)	12.15(04)	11.77(10)	COP
2014 Apr 05.1	+62.5	16.00(04)	15.07(03)	12.93(03)	12.32(02)	11.81(02)	TJO
2014 Apr 07.9	+65.3	...	15.06(12)	13.16(02)	12.40(04)	12.10(02)	COP
2014 Apr 08.9	+66.3	16.25(04)	...	13.10(03)	12.50(03)	12.09(02)	TJO
2014 Apr 09.5	+66.9	...	...	13.12(02)	12.48(05)	11.98(03)	TNT
2014 Apr 11.9	+69.3	16.20(06)	...	13.14(03)	12.58(03)	12.17(02)	TJO
2014 Apr 13.5	+70.9	...	15.15(05)	13.18(02)	12.59(05)	12.12(03)	TNT

Table 2
(Continued)

UT Date	[a]Epoch	U (mag)	B (mag)	V (mag)	R (mag)	I (mag)	Telescope
2014 Apr 17.9	+75.3	16.26(05)	15.27(03)	13.31(03)	12.79(02)	12.36(01)	TJO
2014 Apr 19.5	+76.9	16.55(10)	15.25(03)	13.36(02)	12.79(05)	12.34(03)	TNT
2014 Apr 20.6	+78.0	...	15.29(03)	13.42(02)	12.84(05)	12.44(03)	TNT
2014 Apr 21.6	+79.0	16.55(09)	15.30(03)	13.42(02)	12.85(05)	12.42(03)	TNT
2014 Apr 22.5	+79.9	16.54(09)	15.30(03)	13.46(02)	12.88(05)	12.46(03)	TNT
2014 Apr 24.6	+82.0	16.66(16)	15.29(03)	13.47(02)	12.95(05)	12.52(03)	TNT
2014 Apr 26.6	+84.0	...	15.32(03)	13.56(02)	12.99(05)	12.57(03)	TNT
2014 Apr 27.6	+85.0	...	15.37(03)	13.58(02)	13.03(05)	12.68(03)	TNT
2014 Apr 28.6	+86.0	16.74(07)	15.40(03)	13.61(02)	13.07(05)	12.66(03)	TNT
2014 May 01.9	+89.3	...	15.45(16)	13.60(06)	13.10(07)	12.72(13)	TJO
2014 May 13.6	+101.0	...	15.54(04)	13.95(02)	13.49(05)	13.13(03)	TNT
2014 May 14.6	+102.0	...	15.61(04)	14.03(02)	13.52(05)	13.15(03)	TNT
2014 May 26.6	+114.0	17.55(10)	15.79(02)	14.28(01)	13.82(05)	13.47(03)	TNT
2014 Jun 08.5	+126.9	17.73(18)	...	14.56(02)	14.08(05)	13.88(04)	TNT
2014 Jun 10.9	+129.3	...	15.81(10)	14.49(03)	...	...	COP
2014 Sep 18.2	+228.7	...	17.59(03)	16.67(04)	16.67(06)	16.02(07)	NOT
2014 Oct 27.0	+268.4	...	17.95(03)	17.23(02)	...	...	COP
2014 Oct 30.8	+271.2	...	18.05(06)	17.18(06)	17.18(10)	16.18(12)	LJT
2014 Nov 21.8	+293.2	...	18.62(07)	17.27(12)	17.21(18)	16.22(14)	LJT
2014 Dec 18.9	+320.3	...	18.70(05)	17.96(08)	18.06(13)	16.70(14)	LJT
2014 Dec 20.1	+321.5	...	18.83(05)	17.83(03)	...	...	COP
2015 Jan 19.8	+352.2	...	19.05(03)	18.44(04)	...	...	COP
2015 Jan 22.9	+355.3	...	19.19(06)	18.39(04)	18.31(08)	16.98(10)	LJT
2015 Mar 10.8	+402.2	...	19.91(16)	18.92(10)	...	...	COP
2015 Mar 31.9	+423.3	...	...	19.06(10)	...	...	COP
2015 Apr 11.8	+434.2	...	...	19.10(14)	...	...	COP

Note.
[a] Days after $t_{B\max}$ on 2014 February 02.1 (JD 2456690.1).

(This table is available in machine-readable form.)

Table 3
Log of Observations of SN 2014J with *HST* WFC3/UVIS

Filter	Date of Obs.	Exp. Time (s)	[a]Epoch
F438W	2014 Sep 5 19:12:57	2 × 256	216.2
F555W	2014 Sep 5 19:29:44	2 × 256	216.2
F555W	2015 Feb 2 05:06:06	3 × 128	365.6
F438W	2015 Feb 2 05:24:41	3 × 512	365.6
F555W	2015 Jul 20 01:35:40	3 × 144	533.5
F438W	2015 Jul 20 01:55:15	3 × 448	533.5
F555W	2016 Jan 2 05:29:17	3 × 144	699.6
F438W	2016 Jan 2 06:42:27	3 × 448	699.7
F555W	2016 Jul 2 01:37:07	1720	881.5
F438W	2016 Jul 2 04:07:56	2420	881.6

Note.
[a] Days after $t_{B\max}$ on 2014 February 02.1 (JD 2456690.1).

a given delay time t is

$$F_\lambda(t) = \int_0^t F_{\mathrm{SN},\lambda}(t - t')f(t')dt'. \quad (1)$$

In the above expression, the kernel function $f(t)$ includes all the physical and geometrical information of the dust and is expressed as

$$f(t) = C_{\mathrm{ext}}\omega c \int_{-ct/2}^{+\infty} \frac{\Phi(\theta)}{r} \int_0^{2\pi} n(\varphi, z, t)d\varphi dz\ , \quad (2)$$

where φ and z are defined as in Figure 1 of Patat (2005), C_{ext} is the extinction cross section, ω is the dust albedo, θ is the scattering angle, n is the number density of the dust particles, $r(=z + ct)$ represents the distance between the SN and the dust volume element and $\Phi(\theta)$ is the scattering phase function satisfying $\int_{4\pi} \Phi(\theta)d\Omega = 1$. Both ω and $\Phi(\theta)$ are wavelength-dependent (Weingartner & Draine 2001; Draine 2003).

To obtain the total flux received by the observer, the $F_\lambda(t)$ is added to the flux coming from the SN directly:

$$F_{T,\lambda}(t) = [F_{\mathrm{SN},\lambda}(t)e^{-\tau_d} + F_\lambda(t)]e^{-\tau_I}. \quad (3)$$

Here τ_d is the optical depth of the CSM along the line of sight, while τ_I is the optical depth of the ISM.

3.2. Analytical Fitting

We apply the above model to the light curves of SN 2014J. The shape of $F_{\mathrm{SN},\lambda}(t)$ can be approximately represented by a flux distribution of a unreddened SN with similar $\Delta m_{15}(B)$ and spectral evolution. Srivastav et al. (2016) found that SN 2014J is similar to SN 2003du, except that the latter suffers negligible extinction (Anupama et al. 2005). Therefore we use the B-band light curve of SN 2003du, after shifting the peak magnitude to match the corresponding values of SN 2014J, as an input light-curve template to calculate $F_B(t)$. $F_{T,\lambda}(t)$ is the flux distribution of SN 2014J by definition. Assuming that the Equation (2) is Gaussian, the kernel function $f(t)$ can be simplified as

$$f(t) = \frac{A}{\sigma}\exp\left[-\frac{(t - \tau)^2}{2\sigma^2}\right], \quad (4)$$

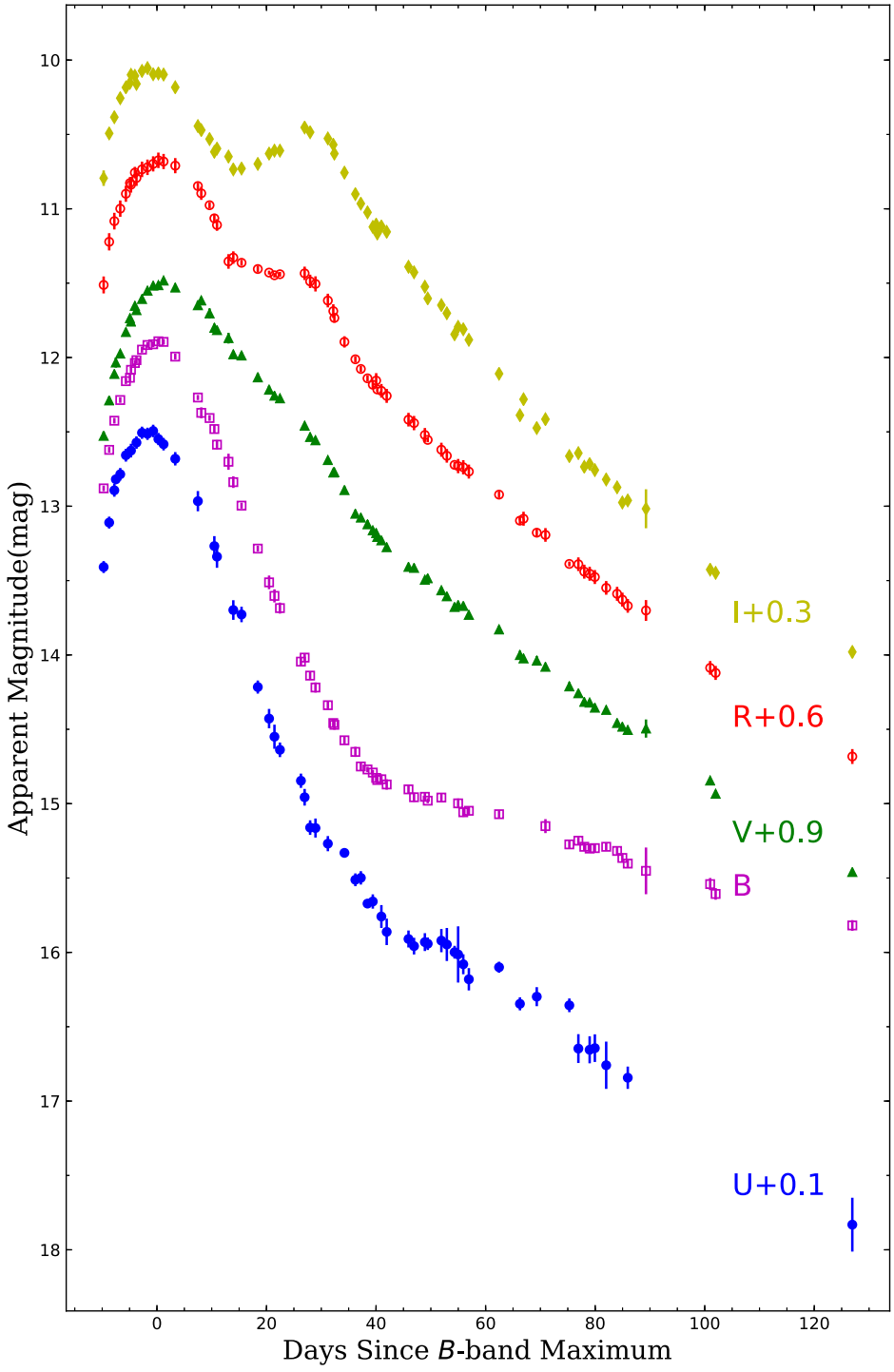
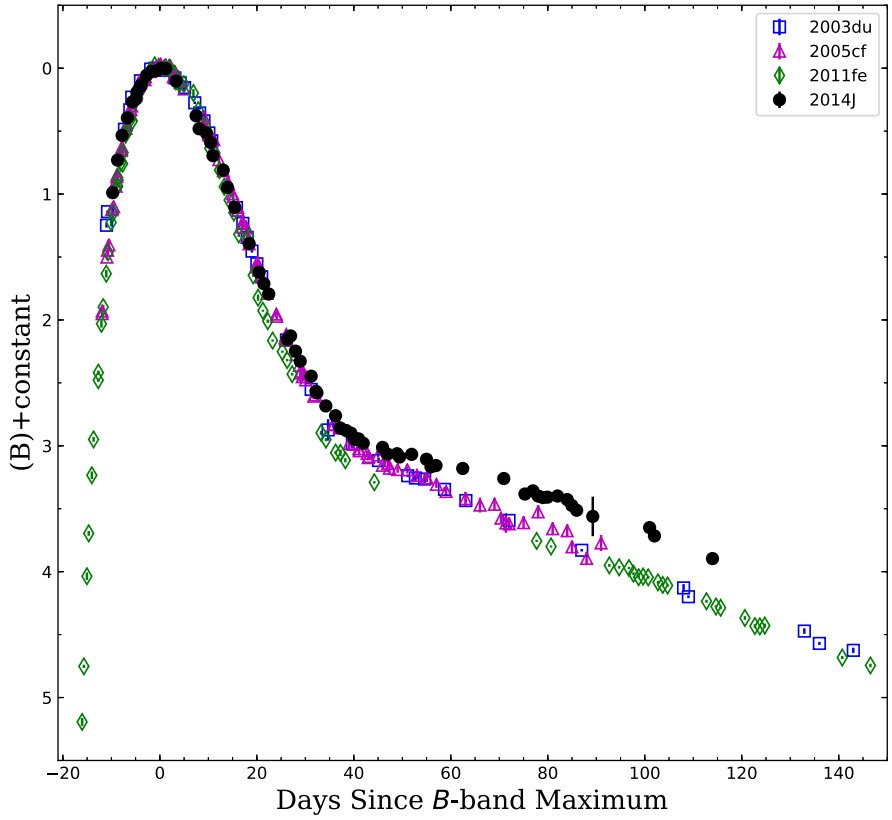


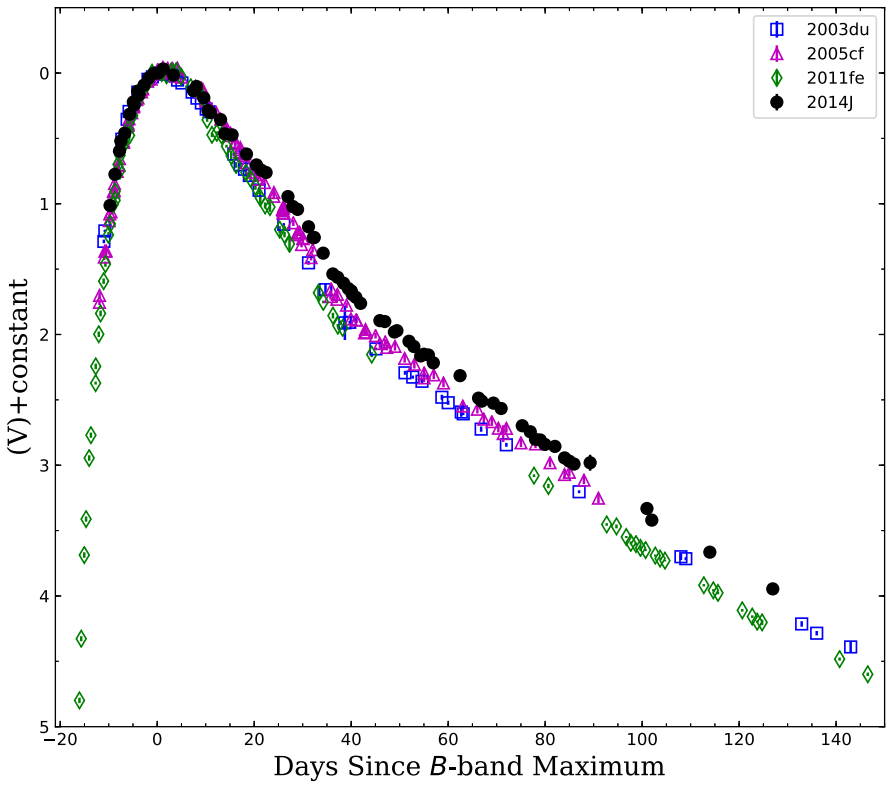
Figure 2. *UBVRI* light curves of SN 2014J, spanning the first 5 months of evolution.

Table 4
HST Photometry of SN 2014J (AB Magnitude)

Epoch	F438W (mag)	F555W (mag)	Δmag/100 days of F438W	Δmag/100 days of F555W
216.2	17.476(0.001)	16.331(0.001)	…	…
365.6	19.672(0.001)	18.668(0.002)	1.47(0.01)	1.57(0.01)
533.5	22.223(0.012)	21.330(0.008)	1.52(0.01)	1.43(0.01)
699.6	24.017(0.031)	22.454(0.023)	1.08(0.03)	0.68(0.02)
881.6	24.988(0.044)	23.513(0.023)	0.53(0.05)	0.58(0.03)



(a) B band



(b) V band

Figure 3. Comparison of the light curves of SN 2014J with SNe 2003du, 2005cf, and 2011fe. The magnitudes are normalized to the peak and the phases are shifted to $t_{B\max}$ for each SN.

Table 5
Decline Rates Measured During 50–110 Days after the *B*-band Maximum Light of SN 2014J

Band	*U*	*B*	*V*	*R*	*I*
Decline Rate (50–110 days) in mag/100 days	2.56 ± 0.08	1.16 ± 0.05	2.50 ± 0.04	2.86 ± 0.03	3.39 ± 0.06

where τ represents the time delay of the arrival of scattered light compared to direct light, which is related to the distance and distribution of the dust. The standard deviation σ is related to the physical size of the dust region responsible for the light echo. A is the scale factor to measure the strength of the light echo. We substitute Equation (4) into Equations (1) and (3) and then fit t in the range of [−8, 150] days.[17]

The best-fit parameters and 1σ error listed in Table 6 are $A = 0.12 \pm 0.03$, $\tau = 64 \pm 8$ days and $\sigma = 26 \pm 8$ days. Hence, we obtain $c\tau = 64 \pm 8$ light days (or $\approx 1.7 \pm 0.2 \times 10^{17}$ cm). Figure 4 shows that the light echo begins to emerge at around 20 days and increases to the peak value (∼30% of total flux) at around 90 days. The distance between the SN and the center of the dust shell is calculated as

$$R = \frac{c\tau}{1 - \cos\theta}. \quad (5)$$

Thus the dust distance from the SN can be estimated as $R > c\tau/2 = 8.3 \pm 1.0 \times 10^{16}$ cm.

More accurate estimation of distance relies on the information about the structure of the dust responsible for the scattering. In our analysis we consider two scenarios in our analysis, spherical shell and disk-like geometry (see Section 3.3, for the latter case). We first assume that the dust cloud is a spherical shell around the SN. According to the fitting result, $f(t > 100\,\mathrm{days}) \ll 10^{-2}$ day^{-1}, the outer boundary of the dust shell is thus inferred as $r_o < 100$ light days (or $<2.6 \times 10^{17}$ cm). Therefore, the dust should be of CS origin. Amanullah & Goobar (2011) suggest that the minimum radius for the CS dust around SNe Ia should be $\sim 10^{16}$ cm because of radiant evaporation. We use the mass limit from Johansson et al. (2017) to calculate the inner boundary radius r_i of the dust shell. The dust shell should be formed by stellar winds and its density $\rho \propto \frac{\dot{M}_{\rm wind}}{v_{\rm wind} r^2}$. Given a mass-loss rate $\dot{M}_{\rm wind} \sim 10^{-7}\,M_\odot$ yr^{-1} (Nomoto et al. 2007) and a stellar wind velocity $v_{\rm wind} \sim 100$ km s^{-1}, the mass of CSM can be expressed as $M_{\rm CSM} = \int_{r_i}^{r_o} \rho dV = \int_{r_i}^{r_o} \frac{\dot{M}_{\rm wind}}{v_{\rm wind} r^2} 4\pi r^2 dr \approx 4 \times 10^{-21}(r_o - r_i)\,M_\odot\,\mathrm{cm}^{-1}$, where r_i is the radius of the inner boundary of the dust shell. The analysis of Johansson et al. (2017) suggests that the pre-existing CSM has a mass $M_{\rm CSM} \leqslant 10^{-5}\,M_\odot$ within $r \sim 10^{17}$ cm. That requires $(r_o - r_i) \leqslant 2.5 \times 10^{15}$ cm, consequently, implying that the dust shell should be very thin. However, putting these estimates and the typical values of $C_{\rm ext}$, ω, $\Phi(\theta)$ (Weingartner & Draine 2001; Draine 2003) and n into Equation (2), the resultant $f(t)$ would be too small to produce a significant light echo, as seen in SN 2014J. Thus, a spherical dust shell seems unlikely for SN 2014J.

[17] In our method, the exponential term of Equation (3) cannot be decoupled with the flux term (i.e., $F_{{\rm SN},\lambda}(t)$ and $F_\lambda(t)$).

Table 6
Best-fit Parameters of Equation (4)

A	τ(days)	σ(days)
0.12 ± 0.03	64 ± 8	26 ± 8

3.3. Monte Carlo Fit

We run a Monte Carlo simulation to fit the *B*-band light curves of SN 2014J. Mie scattering theory (Mie 1908) is used in the calculations of the scattering process (M. Hu 2019, in preparation). Adopting the distribution derived by Nozawa et al. (2015; assuming an average radius for the dust grain of about 0.036 μm), the size distribution of the dust is expressed as

$$f(r) = r^{-a_0} \exp\left[-b_0\left(\log\frac{r}{r_0}\right)^{2.0}\right], \quad (6)$$

where r is the radius of a dust grain, ranging from 5 to 500 nm. We adopt $a_0 = 4.0$, $b_0 = 7.5$ and $r_0 = 0.04\,\mu$m in order to give a size distribution similar to that of Nozawa et al. (2015).

As for the geometric distribution, we consider a disk structure for the dust shell. There are five free parameters to describe the disk (Nagao et al. 2017), including the observing angle $\theta_{\rm obs}$, the opening angle of the disk $\theta_{\rm disk}$, the inner radius $R_{\rm in}$, the width of the CSM $R_{\rm wid}$, and the optical depth in the *B* band τ_B. The radial distribution of the dust density is assumed to have an index $n = -2$ (i.e., $\rho_{\rm dust}(r) = \rho_{\rm dust}(r_{\rm in})(r/r_{\rm in})^{-2}$). The ranges of these parameters are in Table 7. We adopt silicate grains for our dust model. Following the procedure described in Section 3.2, the *B*- and *V*-band light curves of SN 2003du were used as templates in the calculations.

There is a degeneracy between different combinations of the above parameters, i.e., different sets of parameters produce similar light curves. Thus, we list in Table 8 four sets (two groups, Disk 1 and Disk 2 with $\theta_{\rm disk} = 15°$ and 30°, respectively) of parameters, producing light curves similar to SN 2014J.

The *B*-band observed light curve of SN 2014J and the best-fit model are shown in Figure 5. The flux excess in the *B*-band light curve is well fitted by our simulation. The scattered SN light emerges after $t \sim +20$ days, and becomes progressively stronger (Disk 2), reaching its peak around $+80 \sim +100$ days (Disk 1). However, in the *V* band, the scattering effect is much smaller than that seen in the *B* band. The magnitude difference between +10 and +80 days of these two SNe Ia cannot be explained by our model. The scattered light barely affects the light curves at longer wavelengths, as shown in Figures 5(c) and (d). Therefore, we suggest that the diversity of the two SNe in the *R* and *I* bands may be mainly due to their intrinsic specificity. However, we caution that the high degeneracy of our model prevents us from analyzing more quantitatively the CSM distribution. The CSM for such a geometry can be formed when the wind of the red giant companion concentrates

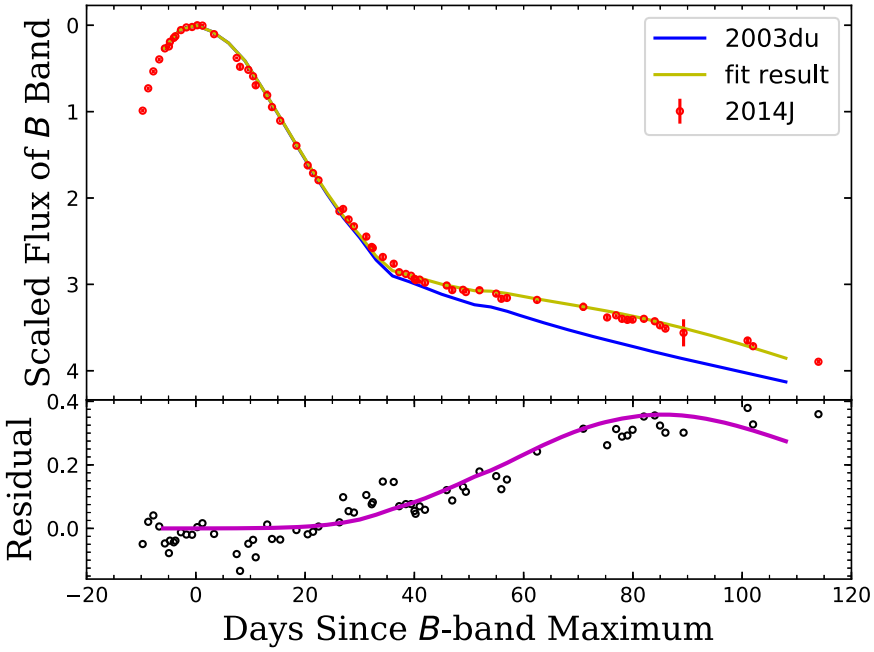


Figure 4. Best fit to the normalized *B*-band light curve of SN 2014J based on the model of dust scattering. The light curves of SN 2014J and SN 2003du are shown (red dots and solid blue curve, respectively). The yellow line represents the light curve of SN 2003du, including the additional contribution of photons scattered by the dust shell located at $\sim 10^{17}$ cm.

Table 7
Parameters of the Dust Structure

Parameter	Range
$\theta_{\rm obs}$	[10°, 60°]
$\theta_{\rm disk}$	[15°, 30°]
$R_{\rm in}$/light day	[20, 110]
$R_{\rm wid}$/light day	[20, 110]
τ_B	[0.2, 2.0]

Table 8
Results from Monte Carlo Simulation

$\theta_{\rm obs}$	$\theta_{\rm disk}$	$R_{\rm in}$/Light Day	$R_{\rm wid}$/Light Day	τ_B
		Disk 1		
30°0	15°	40	40	0.9
60°0	15°	40	40	0.9
		Disk 2		
30°0	30°	110	100	0.6
60°0	30°	110	100	0.6

on the equatorial plane. However, Margutti et al. (2014), Kelly et al. (2014), Pérez-Torres et al. (2014), and Goobar et al. (2014) found the companion of SN 2014J is unlikely to be a red giant star with steady mass transfer or a luminous symbiotic system such as RS Ophiuchi (Dilday et al. 2012). Fainter recurrent novae are still possible candidates for the progenitor system of SN 2014J. On the other hand, some variations of the DD scenario might also form disk-like dusty CSM, e.g., mass outflows during rapid accretion during the final evolution (Guillochon et al. 2010; Dan et al. 2011) and magnetically driven winds from the disk around the WD–WD system (Ji et al. 2013).

4. Nebula-phase Evolution

We examined the very-late-time evolution of SN 2014J, based on the *HST* observations. The images taken with the *HST* WFC3/UVIS in F438W and F555W bands, centering at the position of SN 2014J, are chronologically displayed in Figure 6. In Figure 7, we compare F438W- and F555W-band photometry with the F475W- and F606W-band photometry obtained with *HST* ACS/WFC (Yang et al. 2018a). Our first two epochs photometry are consistent with the values reported in Yang et al. (2017).[18] The *HST* magnitudes obtained in the F555W and F606W bands are in agreement with each other from $t \sim 200$ days to $t \sim 1000$ days, while some discrepancy exists between the F438W- and F475W-band magnitudes.

We combined our data taken after $t \sim$ 300 days with those obtained with the *HST*/WFC mentioned above to construct the pseudobolometric light curve in the wavelength range from ∼3500 to ∼9000 Å, following the same procedure as Yang et al. (2018a) with the warped spectra (see step (5a) in Yang et al. 2018a, Section 3.1). The pseudobolometric light curve is shown in Figure 8. The spectral evolution of SN 2014J is similar to SN 2011fe, and there is only minor evolution between the spectra of SN 2011fe taken at +576 days (Graham et al. 2015a) and +1016 days (Taubenberger et al. 2015) after *B* band maximum. Therefore, we use the spectrum of SN 2011fe at +1016 days to calculate the luminosity of SN 2014J for phases later than ∼+500 days after maximum. The bolometric light curve has been corrected for both the Galactic and host-galaxy extinction, and a distance of 3.53 Mpc (Dalcanton et al. 2009) is adopted in the calculation. The Galactic and host-galaxy extinction have been corrected (see Section 3). The decline rates measured at different phases for SN 2014J are listed in our Table 9, consistent with Table 3 in

[18] The remained discrepancies are mainly due to the difference between Vega and AB magnitude system.

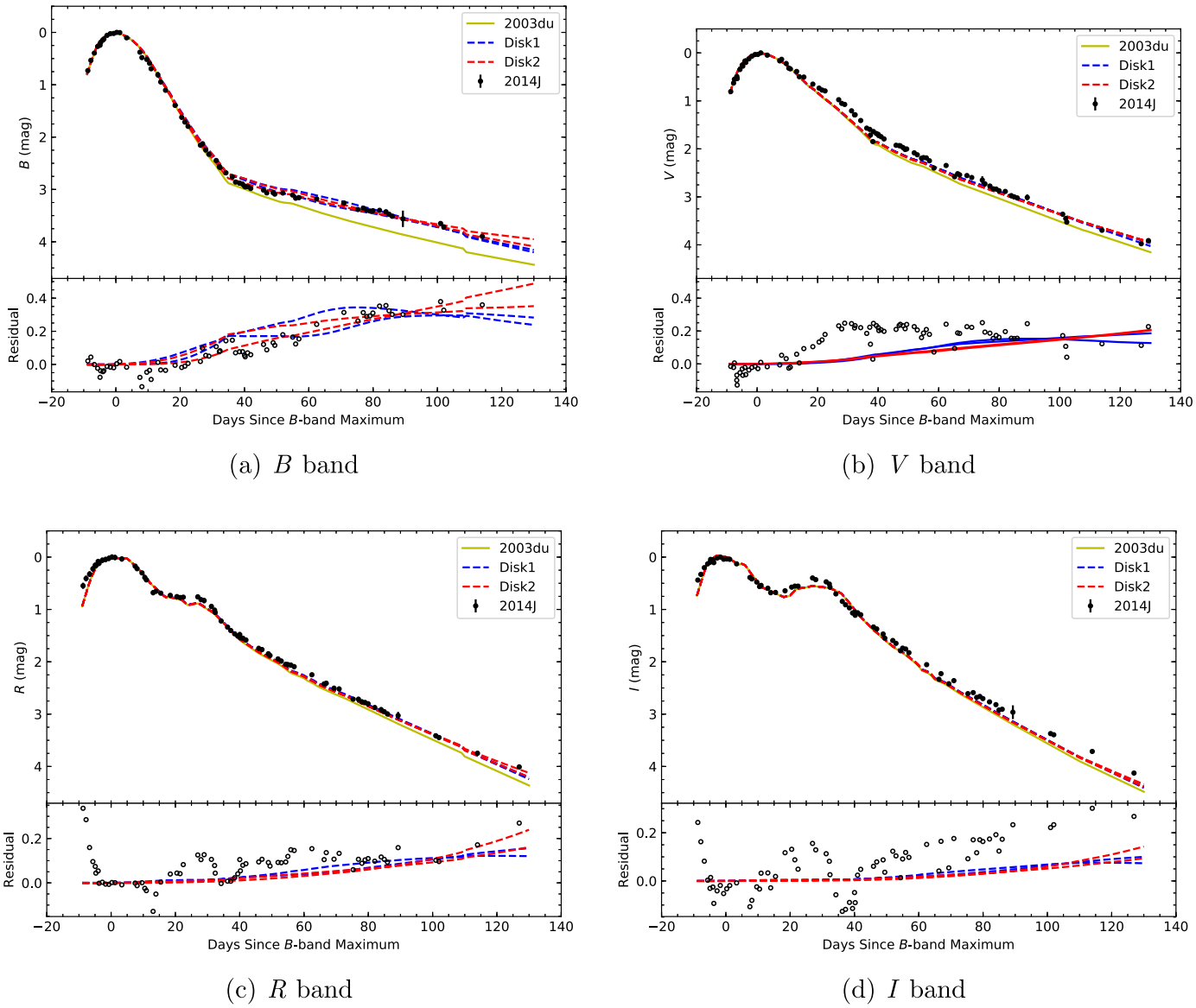


Figure 5. Comparison of the *BVRI*-band light curves of SN 2014J with those derived from Monte Carlo simulations. The black circles in the residual plot in each panel are the magnitude difference between SN 2014J and SN 2003du at similar phases, while the dashed lines represent corresponding magnitude difference between the simulated curves (after considering the effect of dust scattering) and the observed values of SN 2003du.

Yang et al. (2018a). The pseudobolometric light curve of SN 2014J declines over 1.3 mag/100 days, which is faster than the ^{56}Co decay (i.e., 0.98 mag/100 days), from ∼+300 to ∼+500 days. After ∼+500 days, the decline rate decreases to reach 0.40 ± 0.05 mag/100 days when approaching ∼+1000 days after the maximum. The fact that the very-late-time light curve drops slower than the ^{56}Co decay implies that there are other power sources besides radioactive decay energy from ^{56}Co. In the following we analyze these two periods separately.

4.1. Pseudobolometric Light Curve between ∼+300 and ∼+500 days

As shown in Figure 8, the bolometric light curve of SN 2014J declines faster than the ^{56}Co decay. The late-time luminosity evolutions of SN 2011fe (Dimitriadis et al. 2017) and SN 2015F (Graur et al. 2018b) are also shown for comparison. These two SNe also show faster decline rates compared to the ^{56}Co decay during this period. The last measurement (at 1181 days) in Yang et al. (2017) is also plotted in Figure 8. The luminosity evolution of SN 2014J shows a transition at $t \sim +500$ days, also reported for SN 2011fe (Dimitriadis et al. 2017). Before and after this period the light curve declines linearly but with a different rate, as shown in Figure 8. Between ∼+200 and ∼+500 days, SNe Ia are believed to be mainly powered by electron/positron annihilation (Childress et al. 2015). If the positrons are completely trapped by a magnetic field, the decline rate should follow the decay rate of ^{56}Co. The faster decline rate can be explained by a weak or radially combed magnetic field (Milne et al. 1999). However, Crocker et al. (2017) argued that the positron annihilation signal observed in Milky Way requires a stellar source of positrons to have an age of 3–6 Gyr, strongly against significant positron escape in normal SNe Ia. Additionally, previous analysis of late-time observations of SNe Ia does not favor positron escape (Leloudas et al. 2009; Kerzendorf et al. 2014).

An alternative explanation for this faster decline rate is the evolution of emission lines. The nebular-phase spectra of SN

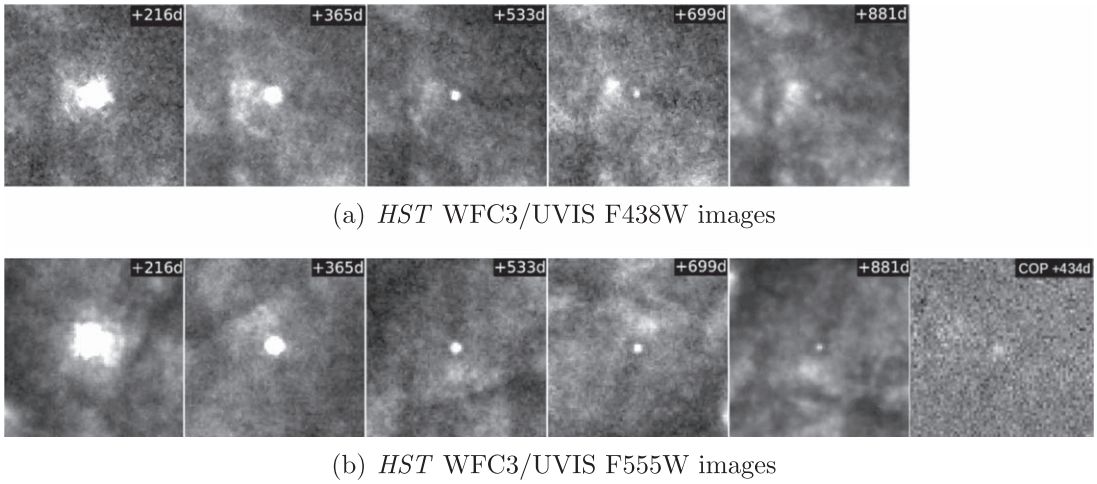


Figure 6. *HST* images of SN 2014J. We label the corresponding phase at the top right corner of each image. The SN can be clearly seen in the images taken as late as +881 days after the *B*-band maximum. The light echo is visible in the bottom left quadrant of the F438W-band images taken on +365 and +533 days. We also display the central part of the latest ground-based, template-subtracted *V*-band image taken with the COP 1.82 m telescope on +434 days in the F555W sequence.

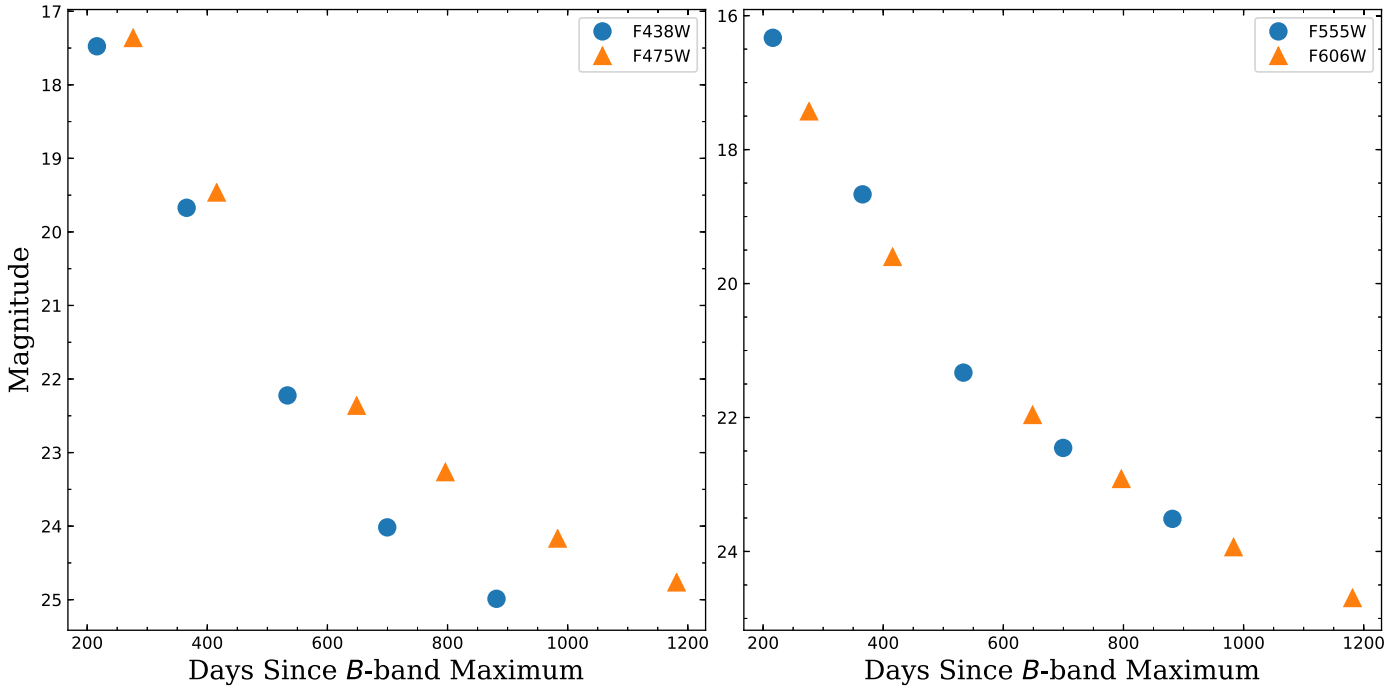


Figure 7. Late-time *HST* photometry of SN 2014J. Left: comparison of the WFC3/UVIS F438W- and ACS/WFC F475W-band photometry. Right: comparison of the WFC3/UVIS F555W-band and ACS/WFC F606W-band photometry.

2014J are available at $t \sim +269$, +351, +428, and +473 days (Srivastav et al. 2016; Zhang et al. 2018), as shown in Figure 9. Overplotted are three nebular spectra of SN 2011fe, taken on +347 days (Mazzali et al. 2015), +463 days (Zhang et al. 2016), and +576 days (Graham et al. 2015a), respectively. All the spectra were downloaded from the WISeREP archive[19] (Yaron & Gal-Yam 2012). All spectra are flux-calibrated using the late-time ground-based and *HST* photometry, with accuracy of about 0.03 mag. At these late phases, the main nebular emission features are blends around [Fe II] λ4400, [Fe III] λ4700, and [Fe II] λ5200. The λ4700 feature tends to become weak in both SN 2014J and SN 2011fe during the period from $t \sim 300$ to $t \sim 500$ days. In the +576 days spectrum of SN 2011fe, this emission completely disappears. Considering the similar spectral evolution of SN 2011fe and SN 2014J, the λ4700 and the λ5200 features should vanish in SN 2014J at a similar phase.

In Figure 10 we over plot the transmission curves of five *HST* filters with the +428 day spectrum, it is evident that the ACS/WFC F775W filter does not cover the fast-evolving spectral features. Thus, the F775W-band light curve is expected to decline at a much slower rate than other bands during this period (see Table 4). Therefore, the evolution of the prominent spectral features can affect the decline rate of the pseudobolometric light curves, which explains the faster decline of the bolometric light curves seen in SN 2014J and SN 2011fe. The ratio of λ4700 and λ5200 emission blends can be considered a proxy of ionization degree. The decrease in the

[19] http://wiserep.weizmann.ac.il/

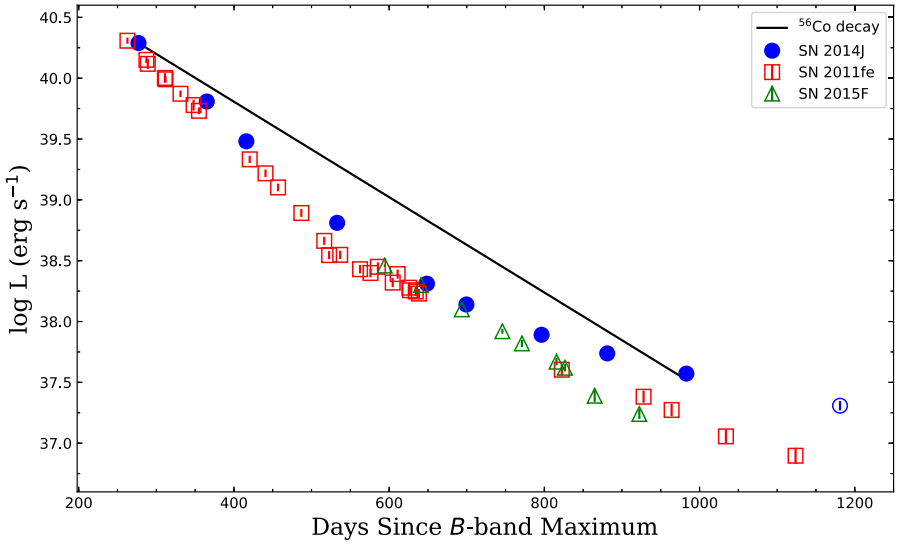


Figure 8. Comparison of the luminosity evolution of SNe 2011fe, 2014J, and 2015F. The black solid line displays the decline rate of pure ^{56}Co decay. The last empty point of SN 2014J is taken from Yang et al. (2017).

Table 9
Late-time Decline Rate of the Bolometric Light Curve of SN 2014J

Period(days)	Decline Rate(Δmag/100 days)
277–365	1.37 ± 0.02
365–416	1.60 ± 0.03
416–533	1.43 ± 0.02
533–649	1.08 ± 0.04
649–700	0.84 ± 0.07
700–796	0.64 ± 0.04
796–881	0.45 ± 0.03
881–983	0.40 ± 0.05

ejecta temperature leads to a smaller ratio of $\lambda4700/\lambda5200$ (and hence a lower ionization).

4.2. Pseudobolometric Light Curve after ∼+500 days

After $t \sim 500$ days, the luminosity of SN 2014J declines more slowly than SN 2011fe and SN 2015F, as well as the ^{56}Co decay, as also noticed by Yang et al. (2018a). However, the complete trapping of positrons cannot explain this flattening in the light curve of SN 2014J. In addition to the decay of ^{56}Co, several energetic mechanisms can affect the late-time evolution. For instance, leptonic energy from Auger and internal conversion electrons produced by the decay chain $^{57}\mathrm{Co} \rightarrow {}^{57}\mathrm{Fe}$ can slow down the late-time bolometric light curve of SNe Ia (Seitenzahl et al. 2009). Besides, the "freeze-out" effect can also have a similar consequence (Fransson & Kozma 1993). If there is a WD companion left after the supernova explosion, the energy released by the delayed radioactive decays of ^{56}Ni and ^{56}Co from the surface of the surviving WD can also contribute to the late-time SN light curve (Shen & Schwab 2017). Finally, a surviving non-degenerate companion after explosion can also contaminatethe late-time light curve (Pan et al. 2012; Shappee et al. 2013). Nevertheless, it is not easy to distinguish different possible scenarios due to the lack of spectra after ∼500 days. Below we explore the possibility that the late-time flattening stems from the long-term decay chain $^{57}\mathrm{Co} \xrightarrow{t_{1/2}=271.8\ \mathrm{days}} {}^{57}\mathrm{Fe}$ and $^{55}\mathrm{Fe} \xrightarrow{t_{1/2}=999.7\ \mathrm{days}} {}^{55}\mathrm{Mn}$.

Because we have no infrared data at late time, we assume the pseudobolometric luminosity to be proportional to the bolometric luminosity. As the ejecta of supernovae expand, the γ-ray optical depth decreases rapidly as t^{-2}, and can be neglected after 600 days (Milne et al. 2001). Therefore, our fit is restricted to data taken after 650 days. Other power sources (light echo, light from the companion, etc.) are not included. The time-dependent contribution expression of each isotope with atomic number A {55, 56, 57} is (Seitenzahl et al. 2014)

$$L_A(t) = 2.221 \frac{\lambda_A}{A} \frac{M(A)}{M_\odot} \frac{q_A^l f_{Al}(t) + q_A^X f_{AX}(t)}{\mathrm{keV}} \times \exp(-\lambda_A t) \times 10^{43}\,\mathrm{erg}, \quad (7)$$

where $\lambda_A = \frac{\ln(2)}{t_{1/2,A}}$, $M(A)$ is the total mass of the element with atomic number A, and q_A^l and q_A^X are the average energies carried by charged leptons and X-rays per decay, respectively. We adopt the values from Table 1 in Seitenzahl et al. (2009), including energies from Auger e^-, internal conversion e^- and e^+. We assume full trapping of the charged leptons and X-rays, thus $f_{Al} = f_{AX} = 1$. In Equation (7) only the $M(A)$ is a free parameter for each isotope.

We then fit the light curve to get the $^{57}\mathrm{Ni}/^{56}\mathrm{Ni}$ mass ratio and compare it with simulations in the literature. First, we regard the masses of all three isotopes as free parameters. The derived $^{57}\mathrm{Ni}/^{56}\mathrm{Ni}$ ratio is 0.124 ± 0.041, which is 5 times the solar value, $(^{57}\mathrm{Fe}/^{56}\mathrm{Fe})_\odot = 0.023$ (Asplund et al. 2009). This value is also much larger than that given by 2D (0.032–0.044; Maeda et al. 2010) and 3D delayed-detonation models (0.027–0.037; Seitenzahl et al. 2013) and the violent merger models (0.024; Pakmor et al. 2012). Additionally, the derived mass of ^{56}Ni, ∼0.18 $M_\odot$ is significantly lower than the typical value of SNe Ia (i.e., about 0.6 $M_\odot$). This means that the full trapping of charged leptons is not a realistic hypothesis.

We account for lepton escape by adopting $f_{Al} = 1 - \exp[-\left(\frac{t_A^l}{t}\right)^2]$, where t_A^l is the time when the optical depth for leptons becomes unity. We choose $t_{56}^l = 249$ days and $t_{57}^l = 812$ days from Case 1 in Dimitriadis et al. (2017). We

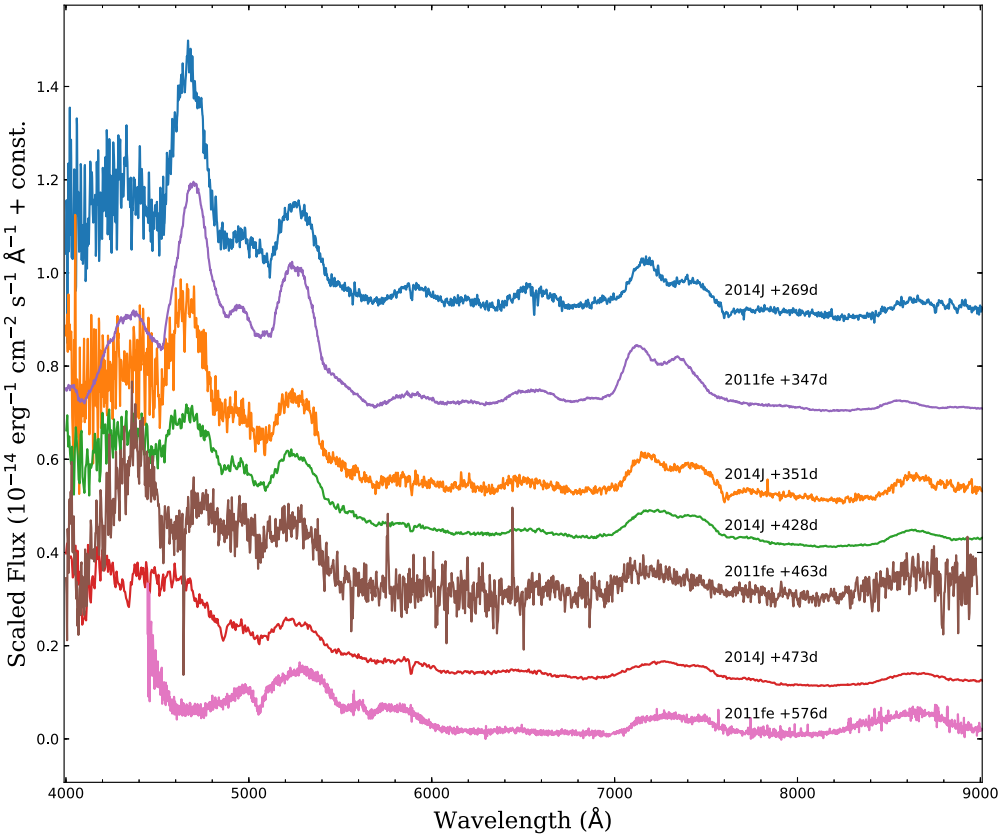


Figure 9. Four late spectra of SN 2014J and three nebular spectra of SN 2011fe. For clarity, the spectra are arbitrarily shifted along the flux axis.

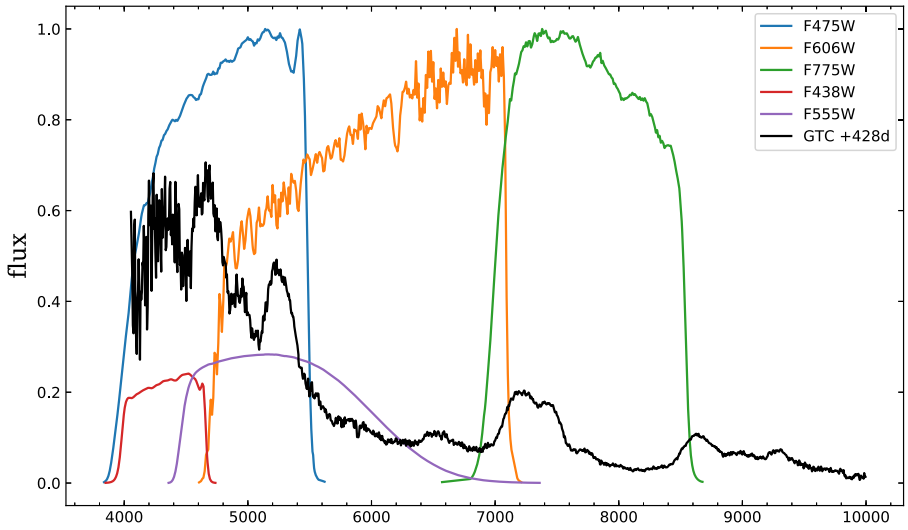


Figure 10. Transmission curves of five *HST* filters, shown with the +428 day GTC spectrum of SN 2014J.

take $t_{55}^{l} = t_{57}^{l}$ because ^{55}Fe and ^{57}Ni both decay without production of positrons (see Table 1 in Seitenzahl et al. 2009). The final fitting result is displayed in Figure 11. Our updated fitting gives $M_{^{56}\mathrm{Ni}} = 0.68 \pm 0.12\ M_{\odot}$ and $^{57}\mathrm{Ni}/^{56}\mathrm{Ni} = 0.035 \pm 0.011$. Our estimate of the mass of ^{56}Ni is fully consistent with the results from Srivastav et al. (2016), Telesco et al. (2015), and Churazov et al. (2014). While the $^{57}\mathrm{Ni}/^{56}\mathrm{Ni}$ ratio is about half of the value reported in Yang et al. (2018a), although they assume no leptons escape and fixed $^{57}\mathrm{Ni}/^{55}\mathrm{Ni} = 0.8$ in their calculations. Our new result is consistent with both the 2D and 3D delayed-detonation simulations mentioned above, but it is inconsistent with the violent merger model.

5. Conclusions

In this paper, we presented extensive photometric observations of SN 2014J collected from numerous ground-based telescopes as well as *HST*. The resulting light curves range from ~ -9 to $\sim +900$ days from the maximum light, representing one of the few SNe Ia with such late-time observations. Our result confirms that SN 2014J is similar to a

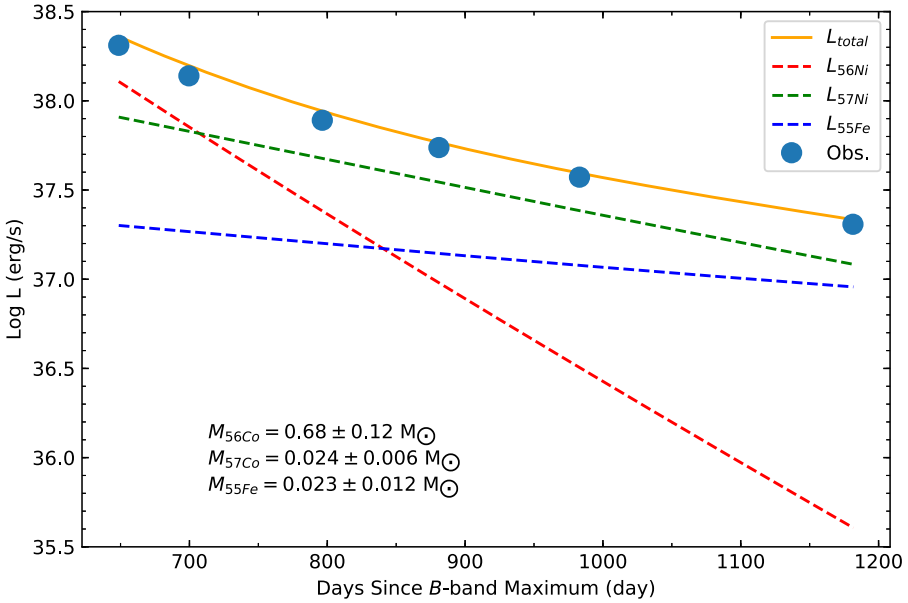


Figure 11. Radioactive decay fits to the late-time pseudobolometric light curve of SN 2014J (open blue circles). The dashed lines are the light-curve contributions of three isotopes. The solid line is the sum of the three isotopes' luminosities.

normal SN Ia around the maximum light, while it is distinguished by prominent blue-band emission in the early nebular phase. This excess emission can be well explained by additional SN light scattered by a disk-like CS dust located at a distance of a few times $\sim 10^{17}$ cm. The CS dust of such a geometry can be formed by faint recurrent novae systems, although some DD scenario channels, such as mass outflows in final evolution or magnetically driven winds from the disk around the WD–WD system, cannot definitely be ruled out.

From $t \sim +300$ to $+500$ days, the luminosity of SN 2014J shows a fast decline compared to the ^{56}Ni decay. After examining the evolution of the late-time spectra, we suggest that this behavior can be attributed to the evolution of [Fe III] λ4700 and [Fe II] λ5200 emissions, instead of positron escape. We further analyze the very-late-time *HST* images of SN 2014J and confirm the late-time flattening of the light curve seen around $t \sim +500$ days. We fit the pseudobolometric light curve using a combination of radioactive decay isotopes ^{56}Ni, ^{57}Ni, and ^{55}Fe. The derived ^{56}Ni mass is in agreement with previous works, and the ^{57}Ni/^{56}Ni ratio is consistent with that predicted by the 2D and 3D delayed-detonation model simulations. Combined with the additional evidence from the excess emission in the blue band in the early nebular phase, we argue that the delayed-detonation through the SD scenario is favored for SN 2014J. However, we caution that without late-time infrared observations, we do not know the real flux fraction of the optical bands, and the pseudobolometric luminosity curve possibly does not represent the real bolometric luminosity evolution. Future late-time photometry and spectroscopy observations, especially those redward of the optical bands, will help to discriminate among the different explosion mechanisms and progenitor systems of SNe Ia.

This work is supported by the National Natural Science Foundation of China (NSFC grants 11325313, 11633002, and 11761141001)), and the National Program on Key Research and Development Project (grant No. 2016YFA0400803). J.-J. Zhang is supported by the National Science Foundation of China (NSFC, grants 11403096, 11773067), the Youth Innovation Promotion Association of the CAS, the Western Light Youth Project, and the Key Research Program of the CAS (grant No. KJZD-EW-M06). T.-M. Zhang is supported by the NSFC (grants 11203034, 11633002). We acknowledge the support of the staff of the Xinglong 80 cm telescope. This work was also partially supported by the Open Project Program of the Key Laboratory of Optical Astronomy, National Astronomical Observatories, Chinese Academy of Sciences. Funding for the LJT has been provided by Chinese Academy of Sciences and the People's Government of Yunnan Province. The LJT is jointly operated and administrated by Yunnan Observatories and Center for Astronomical Mega-Science, CAS.

This paper is based on observations with the 80 cm Joan Oró Telescope (TJO) of the Montsec Astronomical Observatory (OAdM), which is owned by the Catalan Government and operated by the Institute for Space Studies of Catalonia (IEEC).

This work is also based on observations collected at Copernico and Schmidt telescopes (Asiago, Italy) of the INAF—Osservatorio Astronomico di Padova. This paper is also partially based on observations collected at Copernico 1.82 m telescope (Asiago, Italy) of the INAF-Osservatorio Astronomico di Padova; Galileo 1.22 m telescope of the University of Padova; SB and LT are partially supported by the PRIN-INAF 2016 with the project "Toward the SKA and CTA era: discovery, localization, and physics of transient sources." This work is partially based on observations collected at the Copernico 1.82 m telescope (Asiago, Italy) of the INAF —Osservatorio Astronomico di Padova.

N.E.R. acknowledges support from the Spanish MICINN grant ESP2017-82674-R and FEDER funds.

J.I. acknowledges support from the Spanish MINECO grant ESP2017-82674-R.

S.B., L.T., and P.O. are partially supported by the PRIN-INAF 2017 "Toward the SKA and CTA era: discovery, localization, and physics of transient sources" (PI Giroletti).

L. Wang is supported by NSF grant AST-1817099.

F. Huang was supported by the NSFC (11803021), and the Collaborating Research Program (OP201702) of the Key

Laboratory of the Structure and Evolution of Celestial Objects, Chinese Academy of Sciences.

The research of Y. Yang is supported through a Benoziyo Prize Postdoctoral Fellowship.

We are grateful to Georgios Dimitriadis for kindly sharing the spectrum of SN 2011fe.

Software: SWARP (Bertin et al. 2002), SExtractor (Bertin & Arnouts 1996), SCAMP (Bertin 2006), Matplotlib (Hunter 2007), NumPy (van der Walt et al. 2011), SciPy (Oliphant 2007).

ORCID iDs

Xiaofeng Wang https://orcid.org/0000-0002-7334-2357
Jujia Zhang https://orcid.org/0000-0002-8296-2590
Tianmeng Zhang https://orcid.org/0000-0002-8531-5161
Enrico Cappellaro https://orcid.org/0000-0001-5008-8619
Jordi Isern https://orcid.org/0000-0002-0819-9574
Leonardo Tartaglia https://orcid.org/0000-0003-3433-1492
Giacomo Terreran https://orcid.org/0000-0003-0794-5982

References

Amanullah, R., & Goobar, A. 2011, ApJ, 735, 20
Amanullah, R., Goobar, A., Johansson, J., et al. 2014, ApJL, 788, L21
Amanullah, R., Johansson, J., Goobar, A., et al. 2015, MNRAS, 453, 3300
Anupama, G. C., Sahu, D. K., & Jose, J. 2005, A&A, 429, 667
Arnett, W. D. 1979, ApJL, 230, L37
Asplund, M., Grevesse, N., Sauval, A. J., & Scott, P. 2009, ARA&A, 47, 481
Bertin, E. 2006, in ASP Conf. Ser 351, Astronomical Data Analysis Software and Systems XV, 351, ed. C. Gabriel et al. (San Francisco, CA: ASP), 112
Bertin, E., & Arnouts, S. 1996, A&A, 117, 393
Bertin, E., Mellier, Y., Radovich, M., et al. 2002, adass XI, 281, 228
Bonanos, A. Z., & Boumis, P. 2016, A&A, 585, A19
Brown, P. J., Smitka, M. T., Wang, L., et al. 2015, ApJ, 805, 74
Bulla, M., Goobar, A., Amanullah, R., Feindt, U., & Ferretti, R. 2018, MNRAS, 473, 1918
Cao, Y., Kasliwal, M. M., McKay, A., & Bradley, A. 2014, ATel, 5786, 1
Cao, Y., Kulkarni, S. R., Howell, D. A., et al. 2015, Natur, 521, 328
Cappellaro, E., Mazzali, P. A., Benetti, S., et al. 1997, A&A, 328, 203
Cardelli, J. A., Clayton, G. C., & Mathis, J. S. 1989, ApJ, 345, 245
Childress, M. J., Hillier, D. J., Seitenzahl, I., et al. 2015, MNRAS, 454, 3816
Churazov, E., Sunyaev, R., Isern, J., et al. 2014, Natur, 512, 406
Churazov, E., Sunyaev, R., Isern, J., et al. 2015, ApJ, 812, 62
Crocker, R. M., Ruiter, A. J., Seitenzahl, I. R., et al. 2017, NatAs, 1, 0135
Crotts, A. P. S. 2015, ApJL, 804, L37
Dalcanton, J. J., Williams, B. F., Seth, A. C., et al. 2009, ApJS, 183, 67
Dan, M., Rosswog, S., Guillochon, J., et al. 2011, ApJ, 737, 89
Denisenko, D., Gorbovskoy, E., Lipunov, V., et al. 2014, ATel, 5795, 1
Deustua, S. E., Mack, J., Bajaj, V., & Khandrika, H. 2017, WFC3/UVIS Updated 2017 Chip-Dependent Inverse Sensitivity Values, Space Telescope Science Institute Report, ISR 2017-14
Diehl, R., Siegert, T., Hillebrandt, W., et al. 2014, Sci, 345, 1162
Diehl, R., Siegert, T., Hillebrandt, W., et al. 2015, A&A, 574, A72
Dilday, B., Howell, D. A., Cenko, S. B., et al. 2012, Sci, 337, 942
Dimitriadis, G., Foley, R. J., Rest, A., et al. 2019, ApJL, 870, L1
Dimitriadis, G., Sullivan, M., Kerzendorf, W., et al. 2017, MNRAS, 468, 3798
Draine, B. T. 2003, ApJ, 598, 1017
Ferretti, R., Amanullah, R., Goobar, A., et al. 2016, A&A, 592, A40
Foley, R. J., Fox, O. D., McCully, C., et al. 2014, MNRAS, 443, 2887
Foley, R. J., Simon, J. D., Burns, C. R., et al. 2012, ApJ, 752, 101
Fossey, J., Cooke, B., Pollack, G., Wilde, M., & Wright, T. 2014, CBET, 3792, 1
Fransson, C., & Jerkstrand, A. 2015, ApJL, 814, L2
Fransson, C., & Kozma, C. 1993, ApJL, 408, L25
Geier, S., Marsh, T. R., Wang, B., et al. 2013, A&A, 554, A54
Goobar, A. 2008, ApJL, 686, L103
Goobar, A., Johansson, J., Amanullah, R., et al. 2014, ApJL, 784, L12
Goobar, A., Kromer, M., Siverd, R., et al. 2015, ApJ, 799, 106
Graham, M. L., Nugent, P. E., Sullivan, M., et al. 2015a, MNRAS, 454, 1948
Graham, M. L., Valenti, S., Fulton, B. J., et al. 2015b, ApJ, 801, 136
Graur, O. 2019, ApJ, 870, 14
Graur, O., Zurek, D., Shara, M. M., et al. 2016, ApJ, 819, 31
Graur, O., Zurek, D. R., Cara, M., et al. 2018a, ApJ, 866, 10
Graur, O., Zurek, D. R., Rest, A., et al. 2018b, ApJ, 859, 79
Guillochon, J., Dan, M., Ramirez-Ruiz, E., et al. 2010, ApJL, 709, L64
Guy, J., Astier, P., Baumont, S., et al. 2007, A&A, 466, 11
Hachinger, S., Röpke, F. K., Mazzali, P. A., et al. 2017, MNRAS, 471, 491
Han, Z., & Podsiadlowski, P. 2004, MNRAS, 350, 1301
Hosseinzadeh, G., Sand, D. J., Valenti, S., et al. 2017, ApJL, 845, L11
Howell, D. A. 2011, NatCo, 2, 350
Hoyle, F., & Fowler, W. A. 1960, ApJ, 132, 565
Huang, F., Li, J.-Z., Wang, X.-F., et al. 2012, RAA, 12, 1585
Hunter, J. D. 2007, CSE, 9, 90
Iben, I., Jr., & Tutukov, A. V. 1984, ApJS, 54, 335
Isern, J., Jean, P., Bravo, E., et al. 2016, A&A, 588, A67
Ji, S., Fisher, R. T., García-Berro, E., et al. 2013, ApJ, 773, 136
Jiang, J.-A., Doi, M., Maeda, K., et al. 2017, Natur, 550, 80
Johansson, J., Goobar, A., Kasliwal, M. M., et al. 2017, MNRAS, 466, 3442
Jordi, K., Grebel, E. K., & Ammon, K. 2006, A&A, 460, 339
Kasen, D. 2010, ApJ, 708, 1025
Kawabata, K. S., Akitaya, H., Yamanaka, M., et al. 2014, ApJL, 795, L4
Kelly, P. L., Fox, O. D., Filippenko, A. V., et al. 2014, ApJ, 790, 3
Kerzendorf, W. E., McCully, C., Taubenberger, S., et al. 2017, MNRAS, 472, 2534
Kerzendorf, W. E., Taubenberger, S., Seitenzahl, I. R., & Ruiter, A. J. 2014, ApJL, 796, L26
Khokhlov, A. M. 1989, MNRAS, 239, 785
Leloudas, G., Stritzinger, M. D., Sollerman, J., et al. 2009, A&A, 505, 265
Levanon, N., Soker, N., & García-Berro, E. 2015, MNRAS, 447, 2803
Li, W., Wang, X., Vinkó, J., et al. 2019, ApJ, 870, 12
Ma, B., Wei, P., Shang, Z., Wang, L., & Wang, X. 2014, ATel, 5794, 1
Maeda, K., Kutsuna, M., & Shigeyama, T. 2014, ApJ, 794, 37
Maeda, K., Röpke, F. K., Fink, M., et al. 2010, ApJ, 712, 624
Maguire, K., Sullivan, M., Patat, F., et al. 2013, MNRAS, 436, 222
Maoz, D., Mannucci, F., & Nelemans, G. 2014, ARA&A, 52, 107
Margutti, R., Parrent, J., Kamble, A., et al. 2014, ApJ, 790, 52
Marion, G. H., Brown, P. J., Vinkó, J., et al. 2016, ApJ, 820, 92
Marion, G. H., Sand, D. J., Hsiao, E. Y., et al. 2015, ApJ, 798, 39
Mazzali, P. A., Sullivan, M., Filippenko, A. V., et al. 2015, MNRAS, 450, 2631
Mie, G. 1908, AnP, 330, 377
Miller, A. A., Cao, Y., Piro, A. L., et al. 2018, ApJ, 852, 100
Milne, P. A., The, L.-S., & Leising, M. D. 1999, ApJS, 124, 503
Milne, P. A., The, L.-S., & Leising, M. D. 2001, ApJ, 559, 1019
Munari, U., Henden, A., Belligoli, R., et al. 2013, NewA, 20, 30
Nagao, T., Maeda, K., & Tanaka, M. 2017, ApJ, 847, 111
Nomoto, K. 1982, ApJ, 253, 798
Nomoto, K., Saio, H., Kato, M., et al. 2007, ApJ, 663, 1269
Nozawa, T., Wakita, S., Hasegawa, Y., & Kozasa, T. 2015, ApJL, 811, L39
Oliphant, T. E. 2007, CSE, 9, 10
Pakmor, R., Kromer, M., Taubenberger, S., et al. 2012, ApJL, 747, L10
Pan, K.-C., Ricker, P. M., & Taam, R. E. 2012, ApJ, 760, 21
Patat, F. 2005, MNRAS, 357, 1161
Patat, F., Chandra, P., Chevalier, R., et al. 2007, Sci, 317, 924
Patat, F., Chugai, N. N., Podsiadlowski, P., et al. 2011, A&A, 530, A63
Patat, F., Taubenberger, S., Cox, N. L. J., et al. 2015, A&A, 577, A53
Pérez-Torres, M. A., Lundqvist, P., Beswick, R. J., et al. 2014, ApJ, 792, 38
Phillips, M. M., Lira, P., Suntzeff, N. B., et al. 1999, AJ, 118, 1766
Phillips, M. M., Simon, J. D., Morrell, N., et al. 2013, ApJ, 779, 38
Piro, A. L., & Morozova, V. S. 2016, ApJ, 826, 96
Porter, A. L., Leising, M. D., Williams, G. G., et al. 2016, ApJ, 828, 24
Riess, A. G., Filippenko, A. V., Challis, P., et al. 1998, AJ, 116, 1009
Riess, A. G., Filippenko, A. V., Li, W., et al. 1999, AJ, 118, 2675
Röpke, F. K., Kromer, M., Seitenzahl, I. R., et al. 2012, ApJL, 750, L19
Sand, D. J., Hsiao, E. Y., Banerjee, D. P. K., et al. 2016, ApJL, 822, L16
Schlafly, E. F., & Finkbeiner, D. P. 2011, ApJ, 737, 103
Schlegel, D. J., Finkbeiner, D. P., & Davis, M. 1998, ApJ, 500, 525
Seitenzahl, I. R., Ciaraldi-Schoolmann, F., Röpke, F. K., et al. 2013, MNRAS, 429, 1156
Seitenzahl, I. R., Taubenberger, S., & Sim, S. A. 2009, MNRAS, 400, 531
Seitenzahl, I. R., Timmes, F. X., & Magkotsios, G. 2014, ApJ, 792, 10
Shappee, B. J., Holoien, T. W.-S., Drout, M. R., et al. 2019, ApJ, 870, 13
Shappee, B. J., Kochanek, C. S., & Stanek, K. Z. 2013, ApJ, 765, 150
Shappee, B. J., Stanek, K. Z., Kochanek, C. S., & Garnavich, P. M. 2017, ApJ, 841, 48
Shen, K. J., & Schwab, J. 2017, ApJ, 834, 180
Simon, J. D., Gal-Yam, A., Gnat, O., et al. 2009, ApJ, 702, 1157

Siverd, R. J., Goobar, A., Stassun, K. G., & Pepper, J. 2015, ApJ, 799, 105
Soker, N. 2015, MNRAS, 450, 1333
Srivastav, S., Ninan, J. P., Kumar, B., et al. 2016, MNRAS, 457, 1000
Stanishev, V., Goobar, A., Benetti, S., et al. 2007, A&A, 469, 645
Sternberg, A., Gal-Yam, A., Simon, J. D., et al. 2011, Sci, 333, 856
Sternberg, A., Gal-Yam, A., Simon, J. D., et al. 2014, MNRAS, 443, 1849
Taubenberger, S., Elias-Rosa, N., Kerzendorf, W. E., et al. 2015, MNRAS, 448, L48
Telesco, C. M., Höflich, P., Li, D., et al. 2015, ApJ, 798, 93
Terada, Y., Maeda, K., Fukazawa, Y., et al. 2016, ApJ, 823, 43
Vacca, W. D., Hamilton, R. T., Savage, M., et al. 2015, ApJ, 804, 66
van den Heuvel, E. P. J., Bhattacharya, D., Nomoto, K., & Rappaport, S. A. 1992, A&A, 262, 97
van der Walt, S., Colbert, S. C., & Varoquaux, G. 2011, CSE, 13, 22
Wang, B., Meng, X., Chen, X., & Han, Z. 2009, MNRAS, 395, 847
Wang, L. 2005, ApJL, 635, L33
Wang, X., Chen, J., Wang, L., et al. 2018, arXiv:1810.11936
Wang, X., Filippenko, A. V., Ganeshalingam, M., et al. 2009a, ApJL, 699, L139
Wang, X., Li, W., Filippenko, A. V., et al. 2008, ApJ, 675, 626
Wang, X., Li, W., Filippenko, A. V., et al. 2009b, ApJ, 697, 380
Wang, X., Wang, L., Filippenko, A. V., Zhang, T., & Zhao, X. 2013, Sci, 340, 170
Webbink, R. F. 1984, ApJ, 277, 355
Weingartner, J. C., & Draine, B. T. 2001, ApJ, 548, 296
Whelan, J., & Iben, I., Jr. 1973, ApJ, 186, 1007
Yang, Y., Wang, L., Baade, D., et al. 2017, ApJ, 834, 60
Yang, Y., Wang, L., Baade, D., et al. 2018a, ApJ, 852, 89
Yang, Y., Wang, L., Baade, D., et al. 2018b, ApJ, 854, 55
Yaron, O., & Gal-Yam, A. 2012, PASP, 124, 668
Zhang, K., Wang, X., Zhang, J., et al. 2016, ApJ, 820, 67
Zhang, K., Wang, X., Zhang, J., et al. 2018, MNRAS, 481, 878
Zheng, W., Shivvers, I., Filippenko, A. V., et al. 2014, ApJL, 783, L24
Zheng, W., Silverman, J. M., Filippenko, A. V., et al. 2013, ApJL, 778, L15